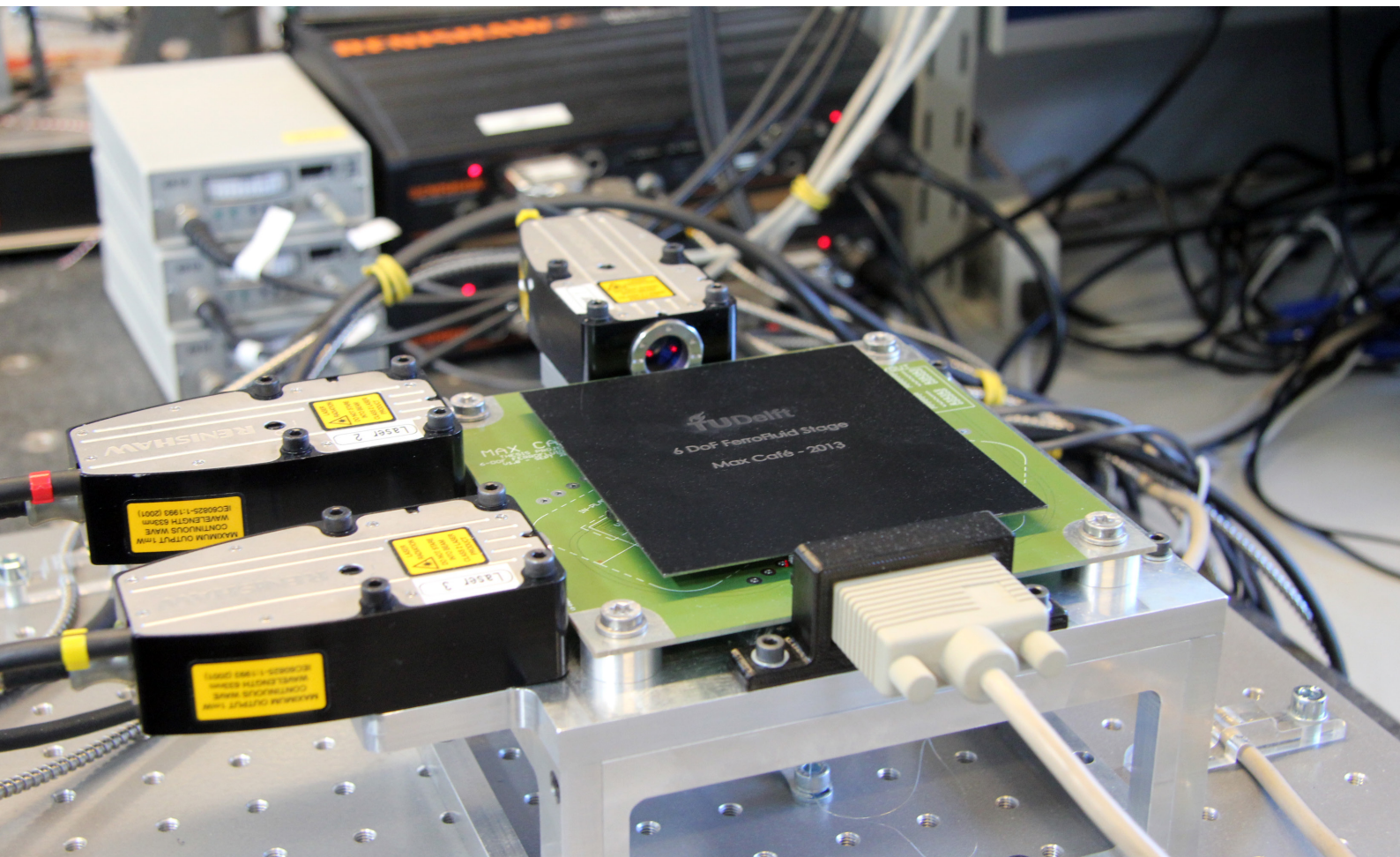


Department of Precision and Microsystems Engineering

Nanometer precision Six Degrees of Freedom Planar Motion Stage with Ferrofluid Bearings

Max Café

Report no : MSD 2014.007
Coach : J.W. Spronck
Professor : R.H. Munnig Schmidt
Specialisation : Mechatronic System Design
Type of report : Master of Science Thesis
Date : 5 May 2014



Nanometer precision Six Degrees of Freedom Planar Motion Stage with Ferrofluid Bearings

MASTER OF SCIENCE THESIS

For the degree of Master of Science in Mechanical Engineering at Delft
University of Technology

Max Café

May 5, 2014

Faculty of Mechanical, Maritime and Materials Engineering (3mE) · Delft University of
Technology



Copyright © Precision and Microsystems Engineering (PME)
All rights reserved.

Glossary of abbreviations

Abbreviations

Symbol	Description
ADC	Analog to Digital Converter
CAS	Cumulative Amplitude Spectrum
CCD	Charge-Coupled Device
CPS	Cumulative Power Spectrum
DAC	Digital to Analog Converter
DoF	Degree(s)-of-Freedom
DSP	Digital Signal Processor
EMF	ElectroMotive Force
FEM	Finite Element Method
FFT	Fast Fourier Transform
FPS	Frames Per Second
MIMO	Multiple Input Multiple Output
PCB	Printed Circuit Board
PI	Proportional and Integral control
PID	Proportional, Integral and Derivative control
PMMA	PolyMethyl MethAcrylate (a transparent thermoplastic)
PSD	Power Spectral Density
PWM	Pulse Width Modulation
RMS	Root Mean Square
SISO	Single Input Single Output
VC-A	Vibration Criterion A

Abstract

This MSc research project is a feasibility study to explore the possibilities of using ferrofluid bearings in high precision, low load applications.

Ferrofluids are fluids containing suspended ferromagnetic particles, which are influenced by magnetic fields due to their ferromagnetic properties. In similarity to for example iron powder, a ferrofluid moves towards the location with the highest gradient of a magnetic field. In the case of permanent magnets, the highest gradients occur on the edges. When the ferrofluid is applied on a magnet, pressure builds up within the ferrofluid, providing the ability to carry a load. In this case the ferrofluid acts as a hydrostatic bearing. The absence of stick-slip in these types of bearings makes them suitable for high-precision positioning systems.

Ferrofluid bearings might typically be applied in precision XY-stages, as are used in biological microscopic research, where it is desired to image a specimen quickly with high resolution. This is commonly achieved by stitching multiple images of roughly 0.1×0.1 mm together to one full image. For this application, actuation in the planar degrees-of-freedom (DoF) is required. Since the ferrofluid bearings do not restrict rotations, all three (instead of two) planar DoF should be actuated. During planar motion, a ferrofluid trail is left behind, thereby lowering the stage with approximately $2 \mu\text{m}/\text{mm}$. When the vertical DoF are also actuated, the stage can bring (and keep) the microscopic sample into focus of the microscope.

In order to apply the ferrofluid bearing to the mentioned microscopic application, a 6 DoF motion stage has been built with a planar range of 10×10 mm and a vertical range of 0.2 mm, see Figure 1. The moving stage has a mass of 0.15 kg, resulting in a steady state ferrofluid-film thickness of approximately $80 \mu\text{m}$.

The stage is actuated by six Lorentz actuators. The magnetic field that is required for the Lorentz actuators is delivered by the same permanent magnets that are used for the ferrofluid bearings. This synergy between bearing and actuator makes the system compact and lightweight. Each magnet delivers the magnetic field for two coils; one for vertical- and one for planar actuation. The six coils of the Lorentz actuators are etched in a 4-layer printed circuit board (PCB). This PCB simultaneously acts as the surface on which the ferrofluid bearings can move. The non-linear position dependency of the actuator-forces is modelled in Matlab and it is verified that this model describes their behaviour with 95% accuracy. This model is also implemented in the control scheme.

Possible microscopic samples can be placed on top of the moving stage. The bottom of this stage (see Figure 2) consists of three magnets, three interferometer mirrors, a PMMA support structure and an iron top-plate. This iron top-plate is used as a target for the capacitive sensors and a flux-path for the magnets, thereby increasing their efficiency.

The Lorentz coils are an inductive load, so feedback current amplifiers are required to drive these loads with a flat (input to force) frequency response. Custom-made amplifiers were designed and manufactured of which the gain and current-limit can be altered easily. Their performance was tested up to 30 kHz, resulting in a flat frequency response and a phase lag of only 5 degrees while the cumulative noise-level up to 1 kHz remains lower than 0.025 mA.

For validation of the system, a capacitive/interferometric measurement system was used to provide position feedback. These high resolution sensors are by far the most expensive components of the setup. In future applications these sensors could be replaced with for example position sensitive detectors (PSDs) and integrated in the same PCB.

The 6 DoF demonstrator stage is a multiple-input-multiple-output (MIMO) system, but decoupling matrices decompose it into six single-input-single-output (SISO) systems, each having their own controller. The control scheme is built in dSPACE, which executes the high-level programming language of Matlab/Simulink.

Open-loop measurements show that up to 500 Hz the planar motion can be treated as a pure mass, so that a simple PID controls are sufficient to control the planar motion up to this frequency. Due to the highly damped vertical motion, a PI-controller is sufficient for out-of-plane control. The behaviour of the demonstrator stage is slightly dependent on its vertical position: when the vertical position is increased, the surface area of the ferrofluid is decreased, causing a lower damping.

Planar steps of 0.1 mm settle within 10 nm in 0.03 seconds. The vertical motion has a control bandwidth of 100 Hz, 250 nm steps in this direction have a settling time (position within $\pm 1\%$ of reference) of 0.02 seconds. These specifications allow the system not only to be used in digital microscopy but also in other applications which require higher specifications, such as white light interferometry, where typical vertical steps of half the light's wavelength (250 nm) are required. The settling times are mainly limited by the maximum force of the actuators. When faster settling times are required in future applications, the system can easily be altered to meet those requirement by adding more layers to the PCB and/or increasing the number windings at each layer.

It can be concluded that a system with ferrofluid bearings can be used in low load applications were fast, high precision positioning is required. The ferrofluid bearings do not seem to limit the precision that is achieved by the demonstrator stage.

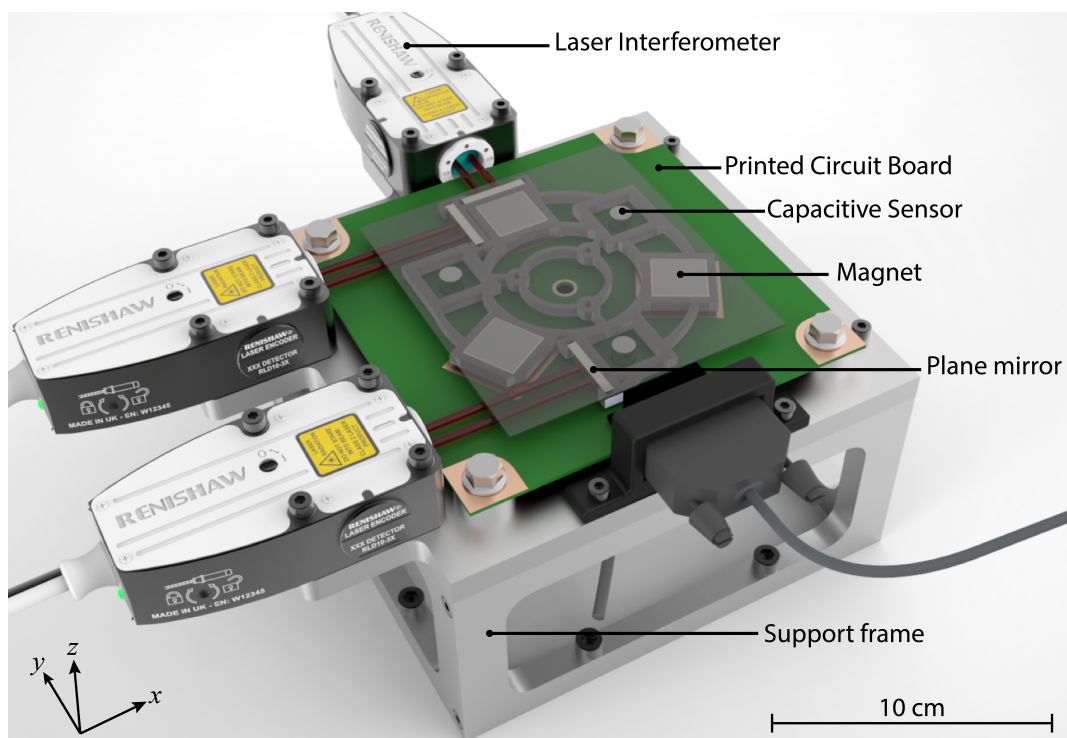


Figure 1: Visualization of the demonstrator stage, showing the PCB with the Lorentz coils, the moving stage with three magnets which contain the ferrofluid, the capacitive sensors and three interferometer mirrors.

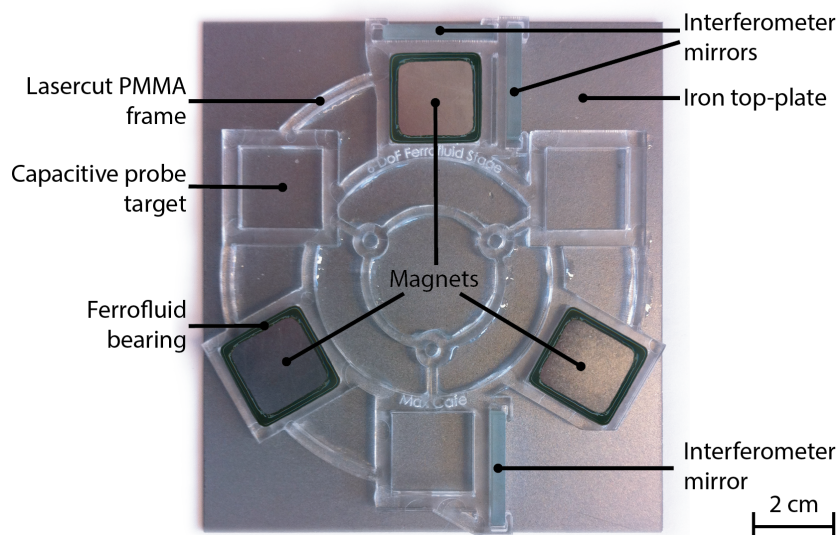


Figure 2: Bottom-view of the moving stage, with the ferrofluid bearings and interferometer mirrors. Possible microscopic samples can be placed on top of this moving stage. The iron top-plate is used as a target for the capacitive sensors and a flux-path for the magnets, thereby increasing their efficiency.

Acknowledgements

Hereby I would like to express my gratitude towards those who contributed directly and indirectly to this thesis:

First and foremost, I wish to thank my supervisor Jo Spronck for all his valuable and constructive suggestions concerning the project and the friendly working environment he created.

Taco Yap, if he would not have been around, I definitely would have had less fun during the (sometimes very tough) graduation hours. He also took the time to review this thesis, for which I am very grateful.

Charlie van der Schoor, thanks to his effort dSPACE is running again. I would like to thank him for his help during the CNC process of several parts (some of them I ended up not using at all!).

Oscar van de Ven and Johan Vogel, they were always willing to answer my questions and I would also like to thank them for reviewing my thesis.

Robert Valk, for helping me with the design of the current amplifiers and the etching of several printed circuit boards.

Rob Munnig Schmidt, for the very educational lectures and masterclasses, and of course taking the time to be chairman of the exam committee.

Manuel Mazo, for taking the time to be part of the exam committee.

Rik van den Hoeven from TNO, for cutting the plane mirrors in the right dimensions (free of charge).

Rob Lutjjeboer, for all his great help in selecting components and supplying the lab equipment.

It is impossible to mention them all, but I express my gratitude towards all my fellow students for the discussions and the good times during the well needed coffee breaks

And last but not least, I would like to thank my parents for their incredible support through all those years.

Table of Contents

Glossary of abbreviations	i
Abstract	ii
Acknowledgements	v
1 Introduction	1
1.1 Ferrofluids	2
1.2 Ferrofluid bearings	3
1.3 Synergy between ferrofluid bearings and Lorentz actuators	4
1.4 Project objectives	4
1.5 Thesis overview	5
2 Requirements	6
2.1 General requirements	6
2.2 Derivation of specifications	7
2.2.1 Initial bandwidth estimation	7
2.2.2 Actuator forces	9
3 Printed Circuit Board (PCB) actuator	11
3.1 Location of the Coils	11
3.2 PCB requirements	12
3.2.1 Perforations to avoid an air-cushion	12
3.2.2 Measures for good heat dissipation	13
3.3 Optimizing the number of windings	13
3.4 PCB build-up	15
3.5 Final design	17
3.5.1 Vertical coils	17
3.5.2 Planar coils	18
3.6 Actuator forces	19

3.6.1	Force transformation matrix	19
3.6.2	Modelling and validation	19
3.7	Temperature measurements	23
3.8	PCB's dynamic deformation	24
4	Moving stage	26
4.1	Description of individual components	26
4.1.1	Iron top-plate	26
4.1.2	PMMA frame	27
4.2	Optimal location of the centre of mass	29
4.3	Dynamic deformation	29
5	Sensors configuration	31
5.1	Capacitive sensors	32
5.2	Laser interferometers	32
5.3	Complete sensor system	33
6	Current amplifiers	35
6.1	Schematic of the current amplifier	35
6.2	Performance	36
6.3	6-in-1 Amplifier assembly	40
7	Control system design	41
7.1	Control hardware	41
7.2	Performance specifications	42
7.3	Introduction to PID control	42
7.4	Planar controllers	43
7.5	Vertical controllers	46
7.6	Additional controller content	48
7.6.1	Position dependent transformation matrix	48
7.6.2	Start-up procedure	48
7.6.3	Safety stop	48
7.6.4	Integral anti-windup	48
8	Performance measurements	50
8.1	Stiffness and damping	50
8.1.1	Vertical stiffness	50
8.1.2	Horizontal and vertical damping	50
8.2	Ferrofluid trail formation	51
8.3	Step response	51
8.4	Positioning precision	53
8.4.1	Planar precision	53
8.4.2	Vertical precision	53
8.5	Specifications of the complete system	55

9	Conclusions	56
10	Recommendations	58
A	Kinematics	60
A.1	Sensor transformation matrix	60
A.2	Modal force transformation	61
B	Additional information	62
B.1	Digital microscopy	62
B.2	White light interferometry	63
B.3	Working principle of a Lorentz actuator	64
C	Influence of an iron plate to the magnetic field	65
D	Resultant force on moving stage	66
E	Modelling the number of windings	67
F	Planar coil concepts	70
G	Production of the stage's frame	72
H	1-DoF Ferrofluid stage	73
H.1	Original 1-DoF stage	73
H.2	Improved 1-DoF stage	73
I	PCB connector and pin-out	77
	Bibliography	78

Chapter 1

Introduction

When it is desired to achieve high accuracies in positioning systems, there are three types of bearings that are commonly used: precision ball bearings, air-bearings, oil-film bearings and magnetic bearings [1]. This research focuses on a relatively new bearing for high precision positioning systems: ferrofluid bearings.

Precision ball bearings have an accuracy that is limited by their mechanical imperfections, these imperfections can cause them to vibrate. High operating speeds can also change properties of lubricating greases, potentially triggering large torque fluctuations.

Air bearings operate with low friction, but they tend to be quite expensive since high geometrical accuracies are required during manufacturing. Also, the supplied pressurized air has to be clean and dry since the small clearances make the bearings susceptible to dust contamination.

Oil film bearings require either oil circulation by an auxiliary pumping system or seals to retain the oil. Problems such as space restrictions, oil leakage and contamination have deterred widespread use of this bearing technology.

Magnetic bearings have a very low and predictable friction, and the ability to run without lubrication and in a vacuum. Passive magnetic bearings use permanent magnets, but are difficult to design due to the limitations described by Earnshaw's theorem, which states that a collection of point charges cannot be maintained in a stable stationary equilibrium configuration solely by the electrostatic interaction of the charges [2]. As a result, most magnetic bearings are active magnetic bearings, using electromagnets which require continuous power input and an active control system to keep the load stable. Other disadvantages include high cost and relatively large sizes.

Ferrofluid bearings do not have the downsides that are mentioned above. Before the working principle of ferrofluid bearings can be explained, as well as their advantages and disadvantages, first the basics of ferrofluids must be discussed.

1.1 Ferrofluids

Ferrofluids consist of three basic components: a base (or carrier) fluid, ferromagnetic particles and a coating on each particle. Liquids like water and various oils are the most common base liquids.

The concentration of the magnetic particles is low, in the range of 3 - 10%. Therefore, many properties of the ferrofluid are similar to those of the base fluid, such as density, vapour pressure and pour point. On the other hand, there is an increase of the ferrofluid's viscosity compared to the viscosity of its base fluid [3]. An external magnetic field also increases the effective viscosity of ferrofluids [4].

The magnetic particles of ferrofluid are usually made of magnetite (Fe_3O_3). With a diameter of around 10 nm, the particles are small enough for thermal agitation to have a significant dispersive influence, thereby stopping the agglomeration which can be observed when for example iron filings are placed in a magnetic field. Particles with such a small size are prevented from sedimentation in a gravitational field because of their thermal energy. This same principle prevents the particles from agglomeration due to magnetic dipole interaction. However, this does not prevent coagulation due to Van der Waals attraction. To overcome this problem, the magnetic particles have a coating (surfactant) which prevents particle-agglomeration. Even when a strong magnetic field gradient is applied to the ferrofluid, no agglomeration is formed [5].

This coating consists of long chained organic molecules, as can be seen in Figure 1.1. A repulsive force is generated by those organic molecules, which prevents the magnetic particles from coming in contact and thus suppresses the destabilizing effect of the Van der Waals interaction. The resulting material behaves like a normal fluid except that it can experience forces due to magnetic polarization.

Ferrofluids are also characterized by their viscosity, which can vary from less than 5 mPa·s to well over 25000 mPa·s depending primarily on the nature of the carrier [6]. The viscosity of the ferrofluid decreases as the temperature increases.

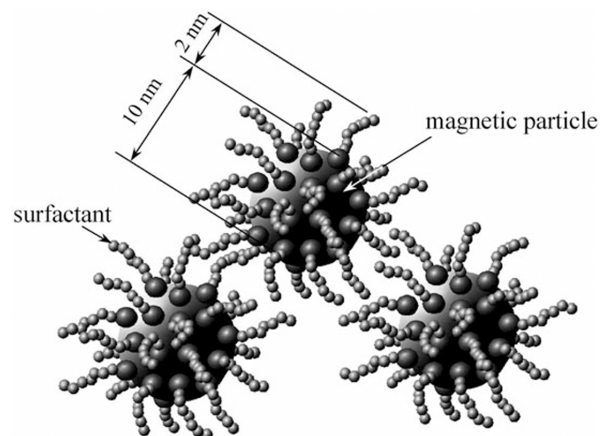


Figure 1.1: Schematic representation of coated magnetic particles in ferrofluid. Figure adopted from Odenbach [7].

1.2 Ferrofluid bearings

Ferrofluids are strongly affected by a magnetic field. In the presence of an uniform magnetic field, the particles in a ferrofluid align with that field. When ferrofluids are exposed to a gradient-field, the particles experience a force such that the fluid itself responds as a homogeneous magnetic liquid which moves to the region of the highest gradient field. In the case of permanent magnets, the highest gradients occur on the edges of the magnet. So when a ferrofluid is applied on a permanent magnet, it will collect on its edges (Figure 1.2a) and pressure builds up within the ferrofluid, this provides the ability to carry a load and thereby creating a ferrofluid bearing [8][9].

The achieved pressure is directly proportional to the product of magnetization of the used ferrofluid and the gradient of the applied magnetic field. The load capacity of a ferrofluid bearing F_{bearing} can be calculated by integrating the pressure p at the bearing's surface S (Figure 1.2b):

$$F_{\text{bearing}} = \iint_S p \, dS \quad (1.1)$$



(a) Ferrofluid moves to the region of the highest gradient field, which is on the edges of a (square) permanent magnet.

(b) The load capacity of a ferrofluid bearing can be calculated by integrating the pressure at the bearing's surface S . The curved lines connect the points of equal pressure (isobars).

Figure 1.2: When a ferrofluid is applied on a permanent magnet it will collect on its edges. Pressure builds up within the ferrofluid, thereby providing the ability to carry a load.

During the translational motion of a ferrofluid bearing, a part of the ferrofluid sticks to the surface on which the bearing moves. In literature, this phenomenon is sometimes referred to as side leakage [10]. Since there is some ferrofluid left behind, the bearing decreases in height during the translational motion. Due to magnetic attraction, the ferrofluid will slowly recollect at the magnet, thereby re-establishing the initial height. That recollection also creates a small planar force. This force makes the integrating action in controllers desirable in order to prevent steady-state errors.

The 'damping-constant' of a ferrofluid bearing not constant, but velocity dependent. In [11] was observed that the damping effect became larger with higher velocities.

1.3 Synergy between ferrofluid bearings and Lorentz actuators

The magnets that are used for the ferrofluid bearings can also deliver the magnetic field for Lorentz actuators. In the case that the reader is not familiar with the working principle of Lorentz actuators, a short introduction can be found in Appendix B.3.

A single magnet can be used to generate a Lorentz force in both vertical and horizontal direction since the magnetic field lines have both a horizontal and a vertical component. This means that one magnet (that also contains ferrofluid) can deliver the magnetic field for two coils; one for vertical- and one for planar actuation. So only 3 magnets are required to actuate the system in 6 DoF.

This synergy between ferrofluid bearings and actuators can keep a motion stage compact and lightweight.

Advantages of a PCB actuator

The traditional actuator coils with copper windings can be replaced with a printed circuit board (PCB) that incorporates the necessary windings as traces on multiple layers of the board.

This approach has a number of advantages over traditional Lorentz actuator designs:

- From a system design point of view, the integration of multiple discrete components adversely affects system reliability, particularly when multiple actuators are required.
- Etching the actuator coils on a PCB gives a lot of engineering freedom (in one plane), so location and width of the coils can be optimized.
- With a given design, the effective length of windings (and thereby the actuator force) can be increased easily by utilizing more PCB layers.
- The ferrofluid bearing system can move directly on the PCB, so no additional flat surface is needed. When the PCB is not flat enough, the vertical actuators can compensate for this.
- PCBs equipped with the required conductive traces can be produced cost effectively using conventional PCB manufacturing techniques.
- Finally, the same PCB might be used to incorporate the sensors and the signal conditioning- and motion control electronics, which reduces the size and price of the overall system.

1.4 Project objectives

Given the physical properties and working principles of a ferrofluid bearing, this project focuses on the feasibility of applying ferrofluid bearings in high precision, planar motion stages. A system containing ferrofluid bearings is theoretically capable of making large planar motions (as long as ferrofluid is available). Such a system might be applied in biological

microscopic research, where it is desired to image a specimen quickly with high resolution. This is commonly achieved by stitching multiple images of roughly 0.1×0.1 mm together to one full image. More information about digital microscopy can be found in Appendix B.1. For these types of applications, actuation in the horizontal degrees-of-freedom (DoF) is required. Since the ferrofluid bearings do not restrict rotations, all three (instead of two) planar DoF should be actuated.

A lot of different applications can be found in the literature concerning ferrofluids [12], but very few are dedicated to planar motion systems. Millet et al. [13] built a 3 DoF displacement stage with, what they call, ferrofluid bubbles as an hydrostatic suspension. However this stage had no closed-loop position controller.

Preliminary research on 3 DoF planar ferrofluid bearings was also done by Morsink et al. [14]. However, this research was inconclusive in proving the capability of precise positioning.

The ability of sub-micrometer positioning was proven by Van Veen [15] for a ferrofluid bearings motion stage with 1 DoF. The same research also proved that planar ferrofluid bearings show no stick-slip and display only viscous friction. Van Veen observed that during the translation, the ferrofluid bearings left a trail of ferrofluid behind, thereby lowering the stage. This research did not address the bearing's behaviour in the other DoF.

The main goal of the current feasibility study is to model, build and test a planar positioning stage with ferrofluid bearings that has a sub-micrometer precision in x , y and z . The actuator coils of the corresponding demonstrator stage will be incorporated in a PCB. The performance related goals of this project are the further investigation of the influence of the trail-formation on the stage's height and the influence of the ferrofluid's damping at different heights of the stage.

1.5 Thesis overview

In Chapter 2 the general requirements for a demonstrator stage with ferrofluid bearings will be deducted with the possible future application of digital microscopy in mind. Six Lorentz actuators are used to actuate the demonstrator stage in six DoF, Chapter 3 describes the modelling and design of those actuators, which are incorporated in a PCB. Possible microscopic samples can be placed on top of the moving stage, Chapter 4 describes the design of that stage. Chapter 5 introduces the capacitive/interferometric measurement system that is used for position feedback. The six Lorentz actuators are an inductive load, so feedback current amplifiers are required to drive these loads with a flat (input to force) frequency response. Chapter 6 describes the design and performance of these current amplifiers. The controller is described in Chapter 7 and the performance of the complete system is discussed in Chapter 8. The conclusions are listed in Chapter 9 and the recommendations in Chapter 10. Multiple appendices on different subjects are also present, and are referred to if more information is necessary about a given subject.

Chapter 2

Requirements

2.1 General requirements

With the possible future application of digital microscopy in mind, the associating requirements can be deducted.

First of all, the demonstrator stage must have a planar operating range of 10×10 mm. During translational motions, the stage must stay within the depth of field of the microscope. The depth of field is the distance between the nearest and farthest objects in a scene that appear acceptably sharp on the image. For a microscope with a numerical aperture (NA) of 1.0 and 100x lens, the typical depth of field is $0.5 \mu\text{m}$ [16].

A planar ferrofluid bearing leaves a ferrofluid trail behind during translational motion, causing the stage to decrease in height. In order to keep the stage within the depth of field during the planar motion, the vertical DoF must also be actuated. However, to ensure only translational motions and no rotations, all 6 DoF must be actuated.

The demonstrator stage will be actuated with PCB Lorentz-actuators, their advantages were described in Section 1.3. Since the surface of a PCB is not perfectly flat, this must be compensated for. The height deviation due to the non-flatness of the PCB and the expected decrease in height due to trail formation are estimated at $15 \mu\text{m}$ and $10 \mu\text{m}$, respectively. Therefore the total required vertical movement is set to $25 \mu\text{m}$. In future applications, the vertical movement might also incorporate autofocus, but for now, no requirements are set regarding this subject.

Furthermore the demonstrator stage must be capable of operating in a normal working environment for optical microscopes without the need of any vibration isolation.

Because microscopy samples are light, the stage has a low load requirement of only 25 grams, but the stage must be able to endure forces due to external shocks or user contact (≤ 10 N).

Requirements:

Degrees of Freedom	6
Load capacity	≥ 25 grams
Range of planar operation	$\geq 10 \times 10$ mm
Range of vertical operation	≥ 25 μm
Precision in planar direction	≤ 500 nm σ
Precision in vertical direction	≤ 100 nm σ
Settling time for 0.1 mm planar step	≤ 0.1 s (position within $\pm 1\%$ of reference)
Settling time for 250 nm vertical step	≤ 0.1 s (position within $\pm 1\%$ of reference)

2.2 Derivation of specifications

This section describes two important specifications that are derived from the general requirements: controller bandwidth and actuator force.

2.2.1 Initial bandwidth estimation

During the imaging process in microscopy, the moving stage (which holds the sample) must stay in place with respect to the microscope, otherwise the images will be blurry. Floor vibrations are the main disturbance source. In order to suppress those floor vibrations, the system needs to provide a virtual connection between the moving stage and the measurement frame, for which a sufficient bandwidth is required.

In the following subsection first an estimation of the expected vibrations is made, with those values the required control bandwidth can be calculated.

Floor vibrations

There are several standards available for the characterization of floor vibrations. A detailed overview of floor vibrations and its characterisations can be found in [17]. In that overview is stated that a commonly used method is based on the BBN criteria, which were proposed by the American high-technology company BBN [18]. The vibration levels of BBN are expressed in velocity and the root mean square (RMS) value for $1/3^{\text{th}}$ octave bands. The criteria apply to floor vibrations in both the vertical and the horizontal directions. The vibration levels are listed for frequencies from 4 to 80 Hz; in [18] is stated that there is significant evidence that vibrations outside these frequencies are rarely a problem.

The requirements state that the demonstrator stage must be capable of operating in a normal working environment for optical microscopes. BBN claims that Vibration Criterion A (VC-A) is adequate in most instances for optical microscopes up to 400x zoom. The corresponding maximum velocity of the expected floor vibrations is 50 $\mu\text{m/s}$, RMS.

Since floor vibrations are of a stochastic nature, the velocity of the BBN curves $v_{\text{BBN}}(f)$ is related to the Power Spectral Density (PSD) of this velocity $S_x(v)$ by the following equation:

$$v_{\text{BBN}}(f) = \sqrt{\int_{-\frac{\sqrt{2}}{2}}^{\frac{\sqrt{2}}{2}} S_x(v) dv} \quad (2.1)$$

The acceleration's PSD $S_x(a)$ is acquired by:

$$S_x(a) = S_x(v) (2\pi f)^2 \quad (2.2)$$

The corresponding PSD ($S_x(a)$) of Vibration Criterion A (VC-A) is displayed in Figure 2.1. From this PSD the worst-case scenario accelerations due to floor vibrations can be calculated. The corresponding RMS acceleration value of VC-A is 37 mm/s^2 .

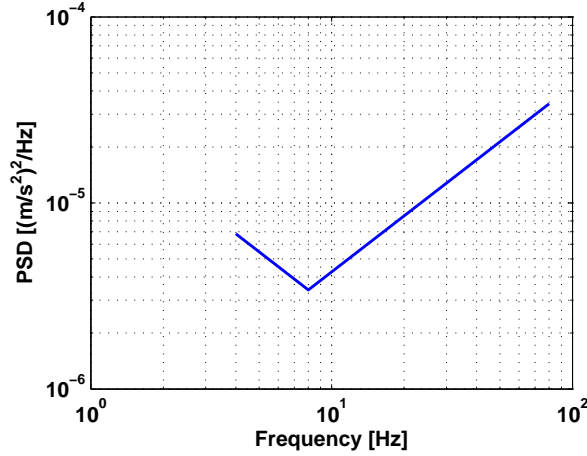


Figure 2.1: Power spectral density of floor vibrations from BBN Vibration Criterion A, which is adequate in most instances for optical microscopes up to 400x zoom.

Controller bandwidth

For the moment we assume that the ground vibrations are the only source of disturbances and the stage has only a mass m and experiences no damping or stiffness. For the first estimation it is assumed that the controller is a simple controller with stiffness k . The control forces F_{control} as a result of the stiffness controller are equal to:

$$F_{\text{control}} = k\varepsilon \quad (2.3)$$

where ε is the tracking error.

If the stage with mass m would perfectly reject all accelerations due to vibrations a_{vib} and follow the reference, the control forces are:

$$F_{\text{control}} = ma_{\text{vib}} \quad (2.4)$$

The controller bandwidth f_{bw} (in Hertz) is:

$$f_{\text{bw}} = \frac{1}{2\pi} \sqrt{\frac{k}{m}} \quad (2.5)$$

Combining Equations 2.3–2.5 yields:

$$f_{\text{bw}} = \frac{1}{2\pi} \sqrt{\frac{a_{\text{vib}}}{\varepsilon}} \quad (2.6)$$

Suppose that in the worst case the stage has the same vibration level as the metrology frame, i.e. $a_{\text{vib}} = 37 \text{ mm/s}^2$. The requirements state that the maximum error in the planar motion $\varepsilon_{x,y}$ is 100 nm and the maximum error in the vertical motion ε_z is 500 nm. When substituting those values in Equation 2.6, the required planar bandwidth $f_{\text{bw},x,y} = 97 \text{ Hz}$ and the vertical bandwidth $f_{\text{bw},z} = 43 \text{ Hz}$ are obtained.

2.2.2 Actuator forces

Disturbance rejection

The expected mass m of the stage is 150 grams and the expected accelerations due to vibrations a_{vib} are 37 mm/s^2 . The required actuator forces F_{vib} for disturbance rejection in x -, y - and z -direction are therefore:

$$F_{\text{vib}} = ma_{\text{vib}} = 0.004 \text{ N} \quad (2.7)$$

The rest of the actuator forces can be divided into planar forces (F_x and F_y) and the vertical forces F_z .

Planar forces

Beside disturbance rejection, the demonstrator stage must also be capable of making a step motion of 0.1 mm within 0.1 seconds. Therefore additional requirements on the actuator force must be set.

In [15] was shown that the planar stiffness of a ferrofluid bearing is close to zero, so the demonstrator stage can be modelled as a mass-damper system, with the corresponding Laplace representation $G(s)$:

$$G(s) = \frac{1}{ms^2 + c_{\text{plane}}s} \quad (2.8)$$

where c_{plane} is the damping in the planar motion.

For a fast step response, the most efficient input-force is a square signal. However, due to the damping this signal is not symmetric in time and therefore has a time offset τ because damping helps in decelerating. In [15] is derived that the required stepping force F_s can be expressed by the following formula:

$$F_s = \frac{c^2 x_s}{m \left(e^{-\frac{ct_s}{m}} - 2e^{\frac{c(\tau-t_s)}{m}} + \frac{c}{m}(2\tau - t_s) + 1 \right)} \quad (2.9)$$

where t_s is the step time, x_s the step size and c the damping constant.

Preliminary results show that $c_{\text{plane}} \approx 20 \text{ Ns/m}$; so for $t_s = 0.1 \text{ s}$ and $x_s = 0.1 \text{ mm}$ the required planar stepping force $F_{s,\text{plane}}$ is 0.022 N.

The total required force for the planar motion F_{plane} is the sum of $F_{s,\text{plane}}$ and F_{vib} :

$$F_{\text{plane}} = F_{s,\text{plane}} + F_{\text{vib}} \quad (2.10)$$

which equals 0.026 N. However, the damping effects and the stiffness of the ferrofluid are a large unknown. The overall safety factor of 5 is therefore used for the calculations of the required force for the planar motion, so F_{plane} becomes 0.13 N.

Vertical forces

In the requirements was stated that a vertical movement of 25 μm is desired due to the non-flatness of the PCB and the expected decrease in height due to trail formation, this means a movement of $\pm 12.5 \mu\text{m}$ around the equilibrium point. The pressure built-up in the ferrofluid results in a vertical stiffness. A preliminary stiffness measurement shows that the expected stiffness of one magnet containing ferrofluid $k_{\text{ff}} \approx 4500 \text{ N/m}$. In Section 1.3 was explained that 3 parallel magnets are required to achieve a 6 DoF motion, so the total expected vertical stiffness k_z is $3k_{\text{ff}}$.

The force F_k to move the stage 12.5 μm in the vertical direction z_s with the vertical stiffness k_z is:

$$F_k = k_z z_s = 0.17 \text{ N} \quad (2.11)$$

In the vertical direction the demonstrator stage must also be capable of making a vertical step z_s of 250 nm within 0.1 s. To calculate the required force $F_{s,\text{plane}}$ again Equation (2.9) can be used. However, the damping in the vertical direction c_{vert} is much higher than the planar damping. Although this damping is highly non-linear, measurements show that a rough estimate of this damping c_{vert} is 3000 Ns/m.

Substituting those values in Equation (2.9), a force $F_{s,\text{vert}}$ of 0.008 N is obtained.

The total vertical force F_{vert} is:

$$F_{\text{vert}} = F_{s,\text{vert}} + F_k + F_{\text{vib}} \quad (2.12)$$

which is roughly 0.18 N. It is clear that the force F_k to move the stage in the vertical direction is the main contributor to the total vertical force F_{vert} .

Again, a safety factor of 5 is used for the calculation of the total vertical force F_{vert} , because the damping effects and the stiffness of the ferrofluid are a large unknown. The total required vertical force F_{vert} becomes 0.90 N.

Printed Circuit Board (PCB) actuator

Six Lorentz actuators are used to actuate the six DoF of the demonstrator stage. The coils of the Lorentz actuators are etched in a printed circuit board (PCB) with four copper layers. This chapter describes the design steps of the complete actuator.

3.1 Location of the Coils

In Section 1.3 was discussed that the magnets that are used for the ferrofluid bearings can at the same time deliver the magnetic field for the Lorentz actuators. This synergy makes the system more compact and lightweight. A single magnet can be used to generate a Lorentz force in both vertical and horizontal direction, so only 3 magnets are required to actuate the system in 6 DoF.

Planar force The vertical component of the magnetic field is of importance to create a planar force, this field is relatively homogeneous directly below the magnet. For a high force-to-current ratio, the optimal location of the windings is therefore just below of the magnet. From a control point of view, it is desired to have a low force-position dependency in the full stroke of the actuator. In order to meet both statements, the optimal location of the windings becomes in the manner as shown in Figure 3.1a. A more detailed explanation can be found in Appendix F. It can be observed that the return path of the windings also have beneficial contribution to the force.

Vertical force The horizontal component of the magnetic field is of importance to create a force in the vertical direction. The horizontal magnetic flux density is highest at the corners of the magnet. In order to generate a high force-to-current ratio, it is therefore desirable to place the windings of the coil as close to these corners as possible. Optimal usage of the magnetic field over the full working area (± 5 mm) is reached when the wires cover at least the area of ± 5 mm from the edges of the magnet. This is illustrated in Figure 3.1b.

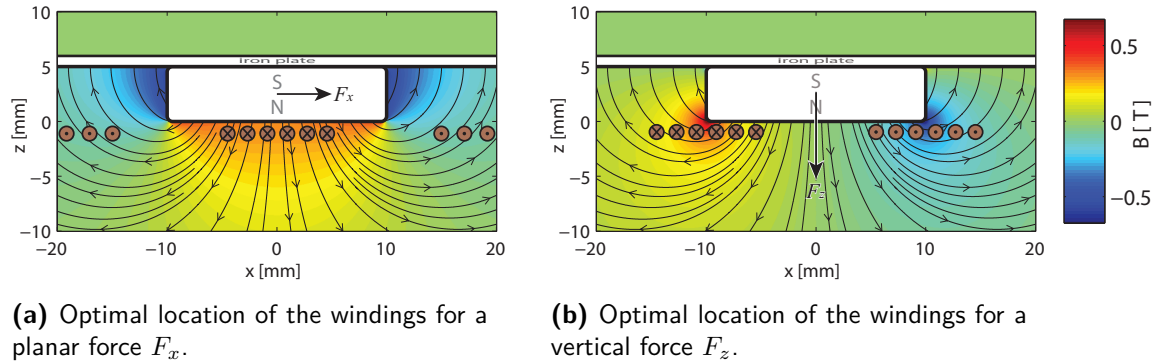


Figure 3.1: One magnet can deliver the magnetic field for two coils; one for vertical- and one for planar actuation. A planar force requires the vertical component of the magnetic field (a) and a vertical force requires the horizontal component of the magnetic field (b). In these figures the magnetic shielding due the iron plate is also visible.

Permanent Magnets The permanent magnets in the Lorentz actuator are made from Nd-FeB. The dimensions are $20 \times 20 \times 5$ mm and they have a mass of 15 grams each. NdFeB magnets have a very high energy product, which makes this type of permanent magnet ideal for providing a high flux density in a small volume.

A drawback of NdFeB magnets is the relatively low demagnetisation temperature (80°C). Since the magnets are thermally connected to the PCB by the (highly thermally conductive) ferrofluid, it is therefore important that the temperature of the PCB stays well below this demagnetisation temperature.

3.2 PCB requirements

The general layout of the PCB has some additional features to ensure that the demonstrator stage operates in a correct manner.

3.2.1 Perforations to avoid an air-cushion

In Section 1.2 was explained that ferrofluid collects at the outer edges of a permanent magnet. This means when a ferrofluid bearing is placed on a flat surface, some air is trapped between the magnet and the ferrofluid. This trapped air acts as an additional spring, increasing the effective stiffness and thereby increasing the load capacity of the bearing. There is also a large disadvantage: when the pressure of the trapped air becomes higher than the ferrofluid pressure, a small amount of air will escape from this cavity. This might happen when a for example a shock-load is applied. This creates a hysteresis effect like a suction cup, resulting in a new equilibrium and a new effective stiffness of the bearing. This behaviour is non-linear and not fully predictable, which makes the system harder to control and this will also result in non-repeatable behaviour and it might even result in controller instability. Van Veen [15] demonstrated that the repeatability is much higher when some perforations are made in the bottom plate, whereby air can easily flow in and out of the cavity. So therefore some perforations are made in the PCB at the location of the magnets.

3.2.2 Measures for good heat dissipation

It is desired to keep the temperature of the PCB below 80 °C to prevent the onset of demagnetization of the magnets.

The PCB has no active cooling, so all heat is removed by convection and conduction. To increase the heat conduction, several measures are taken:

- A PCB consists of a composite of copper foil and glass-reinforced polymer (FR4). Copper has a much higher conductivity (400 W/mK) than FR4 (0.25 W/mK). Therefore all copper layers are connected by so called thermal vias between conductive layers. Thermal vias are created by drilling holes and copper plating them. A detailed description about the optimization of a design with thermal vias can be found in [19].
- The anti-solder mask at the edges is removed, thereby creating a direct connection with the aluminium support frame. Further reading on this support frame can be found in Section 5.3.
- Only the contours of the coils are etched away, therefore leaving the rest of the copper foil intact.

3.3 Optimizing the number of windings

All heat is produced by the coils on the PCB. The dimensions of these coils can be optimized in order to have a heat generation that is as low as possible. The power Q dissipated per coil is:

$$Q = I^2 R \quad (3.1)$$

with R the resistance of the coils and I the required current.

When the width of the windings is decreased, two phenomena take place:

- Less windings \rightarrow thicker windings \rightarrow lower resistance \rightarrow less heat production
- Less windings \rightarrow higher currents are required to create the same force \rightarrow more heat production

The relation between the steady-state temperature characteristics, the track width and the required current to produce the required force was modelled for both planar and vertical coils. A description of this model can be found in Appendix E.

When all constants are eliminated from these formulas of Appendix E, Q becomes only a function of d_{gap} and d_{track} :

$$Q \sim \frac{d_{\text{gap}} + d_{\text{track}}}{d_{\text{track}}} \quad (3.2)$$

This indicates that for a low Q the track width d_{track} must be as large as possible, resulting in high required currents. However, the available power supplies in the lab (Delta Electronics

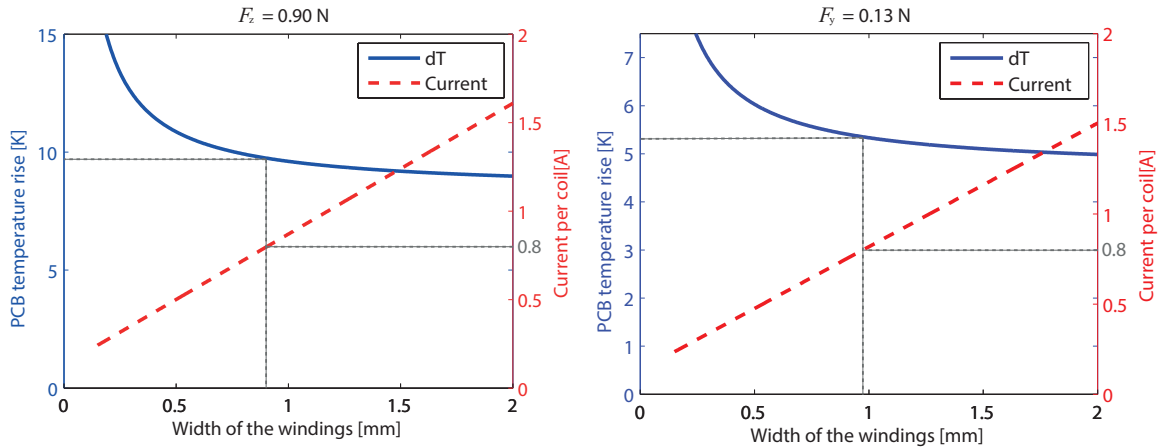
ES 030-5) are only capable of delivering a maximum current of 5 A. This means that 0.8 A is available per coil when this current is equally distributed over all coils.

For good linearity, the total width of the windings of both the vertical as the planar coils must be 10 mm (see Section 3.1). The constraints of the manufacturer state that the insulation width (gap width) d_{gap} must be at least 0.15 mm.

In the requirements of Chapter 2 was stated that the minimum vertical force F_{vert} must be 0.90 N. Each vertical coil therefore has to deliver $0.90/3 = 0.30$ N. For this force, in Figure 3.2a the required width of the windings of the vertical coils is plotted against the expected temperature rise and the corresponding required currents.

The requirements also state a minimum required planar force F_{plane} of 0.13 N. To accomplish this force the y -direction, only two coils (planar coils 2 and 3) are actuated, they each need to deliver a force of $\frac{0.13}{\sqrt{3}} = 0.075$ N. In Figure 3.2b the required width of the windings of the planar coils is plotted against the expected temperature rise and the corresponding required currents.

In both figures can be seen that wider tracks (less windings) lead to a lower temperature rise of the PCB. It can be deduced that for a maximum current of 0.8 A the optimal width of the windings is approximately 0.9 mm for both the vertical and planar coils. The expected corresponding temperature rise of the PCB is 10 °C for the required vertical force and 5 °C for the required planar force. The model did not incorporate the heat-sink capabilities of the moving stage, which is thermally connected to the PCB through the (highly thermally conductive) ferrofluid. Therefore the expected temperature of the PCB will be even lower.



(a) The required currents and expected temperature rise are plotted for several winding widths in the case of $F_{\text{vert}} = 0.90$ N.

(b) The required currents and expected temperature rise are plotted for several winding widths in the case of $F_{\text{plane}} = 0.13$ N.

Figure 3.2: The requirements state the required forces of $F_{\text{vert}} = 0.90$ N and $F_{\text{plane}} = 0.13$ N. A design variable is the width of the windings on the PCB. When this width is varied, this has an influence on the required current and the corresponding expected temperature rise of the PCB. This relationship is plotted for the vertical coils in (a) and the planar coils in (b). The ideal width of the windings, given the power supply's maximum deliverable current of 0.8 A, is approximately 0.9 mm for both the vertical and planar coils. The expected corresponding temperature rises of the PCB are approximately 10 °C and 5 °C, which are well below the requirements.

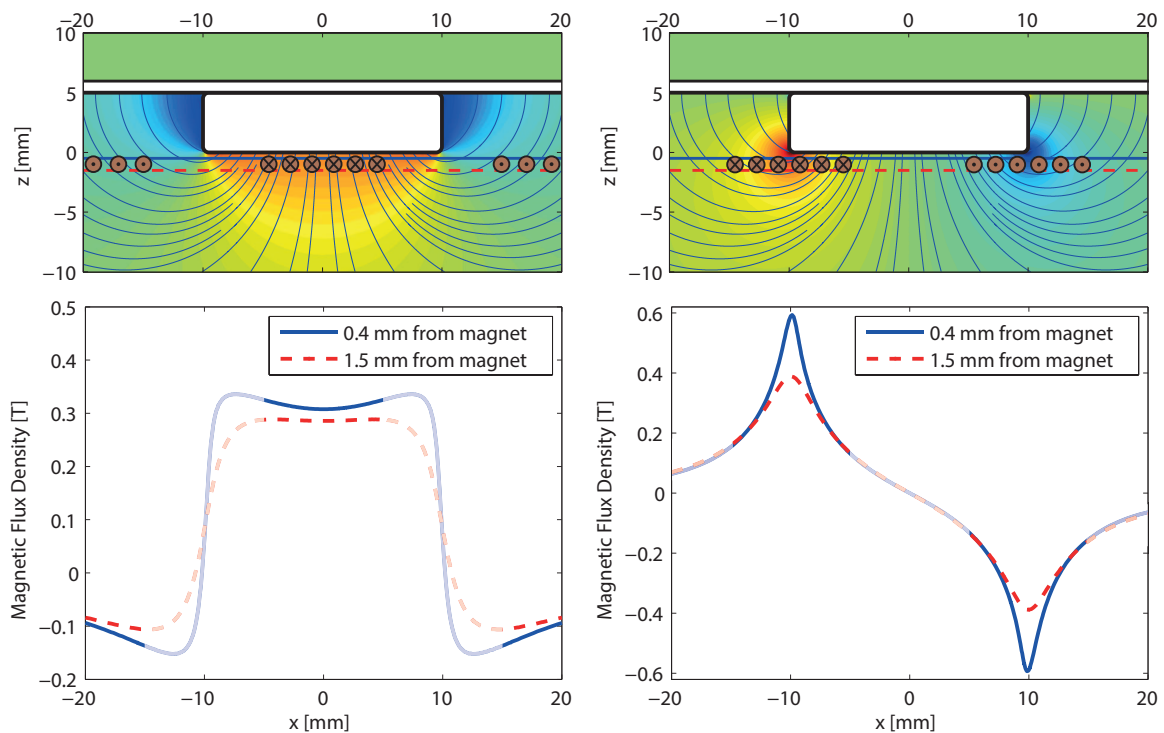
3.4 PCB build-up

In order to create a closed circuit for the coils, each coil needs at least 2 copper PCB layers. Since the planar coils and vertical coils overlap each other, the PCB needs to consist of at least 4 layers. This introduces another design variable: the arrangement of the coils on the different layers. For optimal use of the magnetic field, it is advantageous to find out which coils are more susceptible for a relocation from layers 1&2 to layers 3&4. The cumulative height of those layers is shown in Figure 3.3. Including an estimated ferrofluid-height of 0.2 mm, the average distance between layers 1&2 and the magnet is approximately 0.4 mm, and approximately 1.5 mm for layers 3&4.

Material	Absolute Thickness	Cumulative Thickness
Copper layer 1	0.018 mm	0.018 mm
Prepreg (PR7628)	0.36 mm	0.378 mm
Copper layer 2	0.035 mm	0.413 mm
Core (FR4)	0.71 mm	1.123 mm
Copper layer 3	0.035 mm	1.158 mm
Prepreg (PR7628)	0.36 mm	1.518 mm
Copper layer 4	0.018 mm	1.536 mm

Figure 3.3: PCB board build-up containing the material of the layers including their absolute and cumulative thickness.

In figure 3.4 the magnetic flux density is plotted along the lines of 0.4 mm and 1.5 mm from the magnet. The decrease of the B-field in the vertical component from 0.4 mm to 1.5 mm is 6.5%. However, this decrease is 17.5% for the horizontal component of the B-field. This means that it is advantageous to place the vertical windings (which use the horizontal component of the B-field) on the upper two layers.



(a) Vertical component of magnetic field, which create the planar forces.

(b) Horizontal component of magnetic field, which create the vertical forces.

Figure 3.4: The magnetic flux density at 0.4 mm and 1.5 mm below the magnet of the vertical component of the magnetic field (a) and horizontal component of the magnetic field (b). The decrease of the B-field in the vertical component from 0.4 mm to 1.5 mm is 6.5%. However, this decrease is 17.5% for the horizontal component of the B-field. This means that it is advantageous to place the vertical windings (which use the horizontal component of the B-field) on layers 1&2.

3.5 Final design

The PCB consists of four layers and is designed following the rules of design-classification 6 by Eurocircuits [20], requiring that the track width and insulation width must be at least $150\ \mu\text{m}$. The total size of the PCB is $150\times 150\ \text{mm}$. A DA-15 cable connects the coils with current amplifiers, which will be described in Chapter 6. The PCB consists of three holes through which the capacitive sensors are placed. These capacitive sensors measure the vertical displacements of the moving stage, as will be described in Chapter 5.

3.5.1 Vertical coils

The vertical coils produce the forces in the vertical direction, thereby actuating the 3 out-of-plane DoFs.

Their complete layout is shown in Figure 3.5. The windings have a width of $0.9\ \text{mm}$ and have an (insulating) gap of $0.150\ \text{mm}$. The centre of the coils is $40\ \text{mm}$ distanced from the centre of the PCB, with an angle of 120° between them. The resistance of these coils is $1.1\ \Omega$, the inductance is $3.1\ \mu\text{H}$.

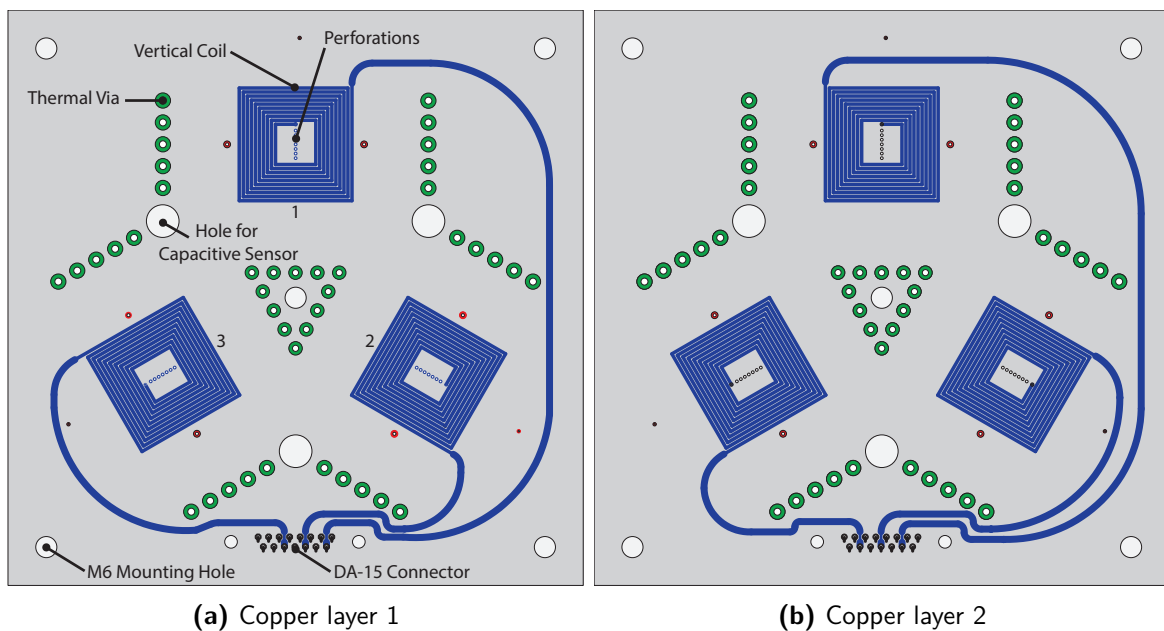


Figure 3.5: Copper layer 1 (a) and copper layer 2 (b) contain the vertical coils. The thermal vias are also highlighted, they create a thermal connection between the different layers to increase heat transportation.

3.5.2 Planar coils

The planar coils generate the planar forces, they are located on layer 3 and 4 as was described earlier. Their complete layout is shown in Figure 3.6. The centre of the coils is 40 mm distant from the centre of the PCB, with an angle of 120° between them. The windings of the those planar coils consist of two parts: the force generating part and the return path.

The force generating part is located directly below the magnet, where the vertical component of the magnetic flux density is highest. The windings have a width of 0.9 mm and have an (insulating) gap of 0.150 mm.

The return path is located further away from the magnet and has a low contribution to the planar force. These parts of the windings can have a larger diameter, because they are not restricted to the width of 10 mm to provide more linearity to the system. A larger coil diameter means a lower resistance, which leads to less heat production. These outer windings all have an equal width of 1.8 mm, this is the maximum width at which the windings of the separate coils do not touch each other.

The resistance of these coils is 1.2Ω and the inductance is $4.3 \mu\text{H}$.

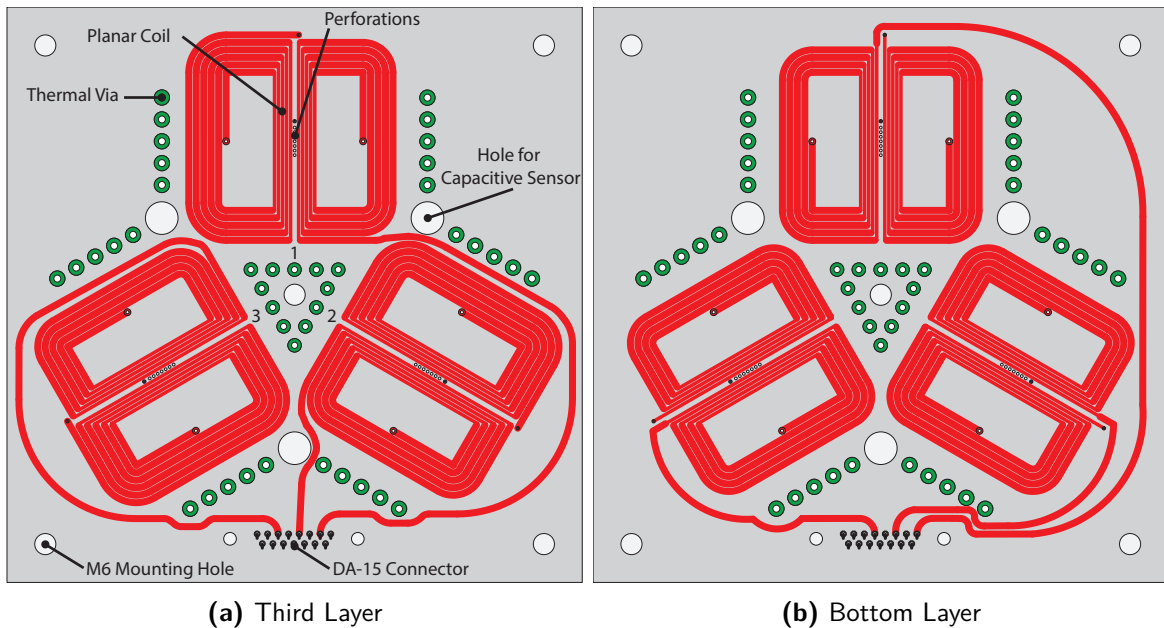


Figure 3.6: Copper layer 3 (a) and copper layer 4 (b) contain the planar coils.

3.6 Actuator forces

One of the key parameters that define the actuator's performance is its motor- or force-constant k_t . This parameter allows one to predict the additional force generated by the actuator for every unit increase in current.

This section describes that this motor-constant is not constant over the range of the actuator and discusses the theoretical modelling and experimental validation of this position-dependency.

3.6.1 Force transformation matrix

The six coils of the PCB actuator work together to generate forces and torques relative to the coordinate system. These forces and torques are combined into one modal force matrix \mathbf{F} :

$$\mathbf{F} = \begin{bmatrix} F_x & F_y & F_z & T_x & T_y & T_z \end{bmatrix}^T \quad (3.3)$$

Since each coil needs a certain current to drive the stage with the correct forces \mathbf{F} , a force-transformation matrix $\Phi_{\mathbf{F}}$ is required that converts these forces into the corresponding actuator currents \mathbf{I} :

$$\mathbf{I} = \Phi_{\mathbf{F}} \mathbf{F} \quad (3.4)$$

where \mathbf{I} describes the individual currents through each coil:

$$\mathbf{I} = \begin{bmatrix} I_{\text{plane1}} & I_{\text{plane2}} & I_{\text{plane3}} & I_{\text{vert1}} & I_{\text{vert2}} & I_{\text{vert3}} \end{bmatrix}^T \quad (3.5)$$

$I_{\text{plane1,2,3}}$ are the required currents through planar coils 1, 2 and 3, whereas $I_{\text{vert1,2,3}}$ are the required currents through vertical coils 1, 2 and 3.

The forces and torques produced by the coils are depended on the magnetic field and therefore on the position of the stage (on which the magnets are mounted). Each possible position of the stage therefore has his own force-transformation matrix $\Phi_{\mathbf{F}}$, which makes $\Phi_{\mathbf{F}}$ position dependent. Therefore Equation (3.4) becomes:

$$\mathbf{I} = \Phi_{\mathbf{F}}(x, y) \mathbf{F} \quad (3.6)$$

3.6.2 Modelling and validation

The position dependent force-transformation matrix $\Phi_{\mathbf{F}}(x, y)$ describes the cross-coupling between the different actuators and the force they deliver. In the symmetrical centre position of the PCB ($x=0, y=0$), there is no cross-coupling between the different actuators. At this position the motor constant of the vertical coils $k_{t,\text{vert}}$ is 0.39 N/A and the motor constant of the planar coils $k_{t,\text{plane}}$ is 0.15 N/A. However, when the system moves towards the outer corners, some cross-coupling arises: the planar coils start producing a (parasitic) vertical Lorentz force and the vertical coils start producing a horizontal Lorentz force. This behaviour is modelled with a combined model of COMSOL and Matlab.



Figure 3.7: The actuator forces and torques were measured with a 6-DoF force sensor. One side of this sensor was mounted to the moving stage and the other side to the measurement frame by means of a temporary support structure.

To validate this model, the model is compared to measurements with a 6-DoF force sensor. One side of this sensor was mounted to the moving stage (see Figure 3.7.), the other side to the measurement frame by means of a temporary support structure.

Measurements were performed at 7 locations along the x -axis and 7 locations along the y -axis. At each location, the six actuators were switched-on one by one and the forces were measured. In this way a *measured* force-transformation matrix $\hat{\Phi}_{\mathbf{F}}(x, y)$ was constructed at each location.

The error between the model and the measurements is calculated in the following way: First, at each of the measured locations, the *modelled* actuator currents are calculated for a force F_u in x -, y - and z -direction. These (modelled) currents \mathbf{I} are then converted back to forces by multiplying those currents with the inverse of the *measured* force-transformation matrix $\hat{\Phi}_{\mathbf{F}}^{-1}$. The corresponding equation becomes:

$$\Delta \mathbf{F} = \hat{\Phi}_{\mathbf{F}}^{-1} (\Phi_{\mathbf{F}} \mathbf{F}) \quad (3.7)$$

The corresponding error vector \mathbf{E} is illustrated in Figure 3.8 and calculated by:

$$\mathbf{E} = \frac{\sqrt{(\Delta F_x)^2 + (\Delta F_y)^2 + (\Delta F_z)^2}}{|\mathbf{F}|} \quad (3.8)$$

with $|\mathbf{F}|$ the magnitude vector of the modelled force.

The mean of the error vector \mathbf{E} at each of the measured locations is 5% with a maximum error of less than 13%. The difference between the modelled forces and measured forces is probably caused by the fact that the magnets have a slightly different remanence than stated on their specifications and/or the location of the stage was slightly different than assumed during the force measurements due to mounting uncertainties.

In order to get more insight into the origin of the cross-coupling between the coils and the magnitude of the required currents, an illustrative example for a force in the y -direction F_y is given below.

Illustrative Example

In this example a force F_y of 0.1 N is required at different locations along the y -axis.

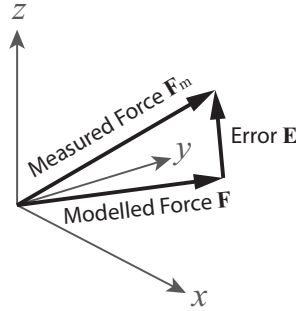


Figure 3.8: The error vector \mathbf{E} between the modelled forces \mathbf{F} and the measured forces \mathbf{F}_m has an average value of 5%.

In the centre position ($x=0, y=0$), there is no cross-coupling, so only planar coils 2 and 3 need to deliver a force. The required currents are:

$$\mathbf{I} = \begin{bmatrix} 0 & -0.39 & 0.39 & 0 & 0 & 0 \end{bmatrix}^T$$

When the stage moves away from its centre location, some cross coupling between the actuators arises: since the planar coils are no longer in the centre of the magnets, an additional (parasitic) vertical force is produced by the planar coils. This means that the vertical coils need to be actuated in order to correct for this. For example in the centre-right position ($x=5, y=0$) the corresponding currents through the coils are:

$$\mathbf{I} = \begin{bmatrix} 0 & -0.39 & 0.39 & 0 & -0.05 & 0.05 \end{bmatrix}^T$$

To give an impression of the relation between the measured force-transformation matrix $\hat{\Phi}_{\mathbf{F}}(x, y)$ and the theoretical force-transformation matrix $\Phi_{\mathbf{F}}(x, y)$, the required currents to achieve a pure force in the y -direction F_y of 0.1 N are displayed in Figure 3.9 for different locations of x . The cross-coupling between the planar and vertical coils is also visible: when the stage moves towards its outer positions, a small vertical force is required in order to maintain a pure F_y .

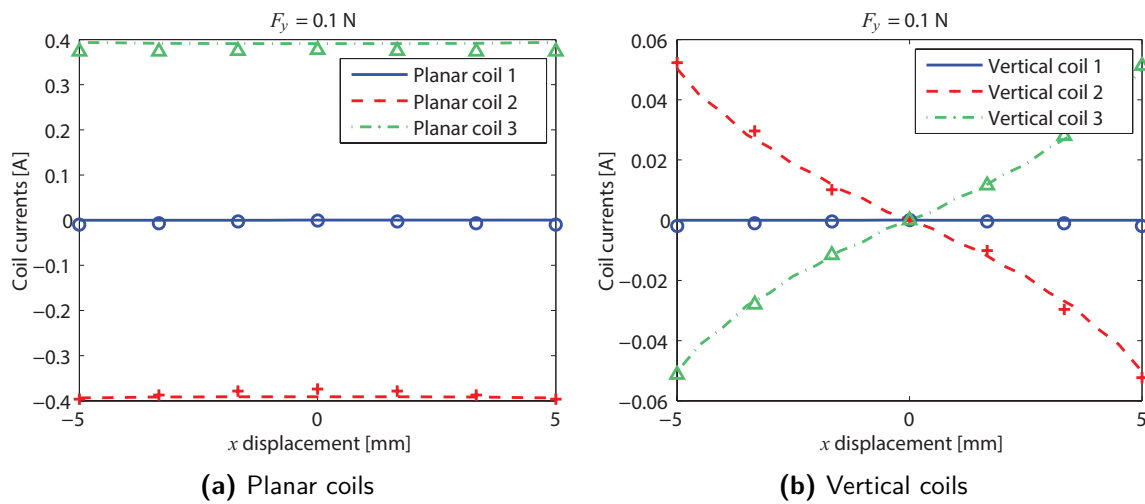


Figure 3.9: The required currents through the coils to deliver a force F_y of 0.1 N are plotted as a function of the x -position of the stage ($y = 0$ and $z = 0$). The theoretical values are displayed with lines and the measured values with symbols. The position dependent cross-coupling between the planar and vertical coils is visible: small vertical forces are required in order to maintain a pure F_y .

3.7 Temperature measurements

It is required to keep the temperature of the magnets below 80 °C to prevent the onset of demagnetization. Since the magnets are thermally connected to the PCB via the ferrofluid, the temperature of the PCB must not exceed this temperature.

The thermal behaviour of the PCB is measured with a FLIR A300 thermal camera, which uses a microbolometer for contact-less measurements of the temperature distributions.

In Figure 3.10 the steady-state thermal images of the PCB are shown for the case where the coils are provided with a current of 1 A, which equals a power input of 1.1 Watt for the vertical coils and 1.2 Watt for the planar coils. The planar coils are located at the bottom two layers of the PCB, therefore the thermal images were also captured with a bottom-view of the PCB.

In both cases the temperature stays well below the required temperature of 80 °C. In normal operation, the expected PCB temperatures will be much lower, since only small forces are required for disturbance rejection. Only during a step motion of the stage, momentarily higher currents are required. Moreover, these measurements were performed without the ferrofluid stage on top of the coils. The moving stage is thermally connected to the coils through the (highly thermally conductive) ferrofluid, so this moving stage can also act as a heat sink. The temperature of the coils will therefore be even lower when the demonstrator stage is in full operation.

Planar coil 2 and vertical coil 2 (which are located below each other) appear somewhat warmer than the other coils. This temperature deviation is probably caused by some imperfections in the insulating layers in between the copper layers.

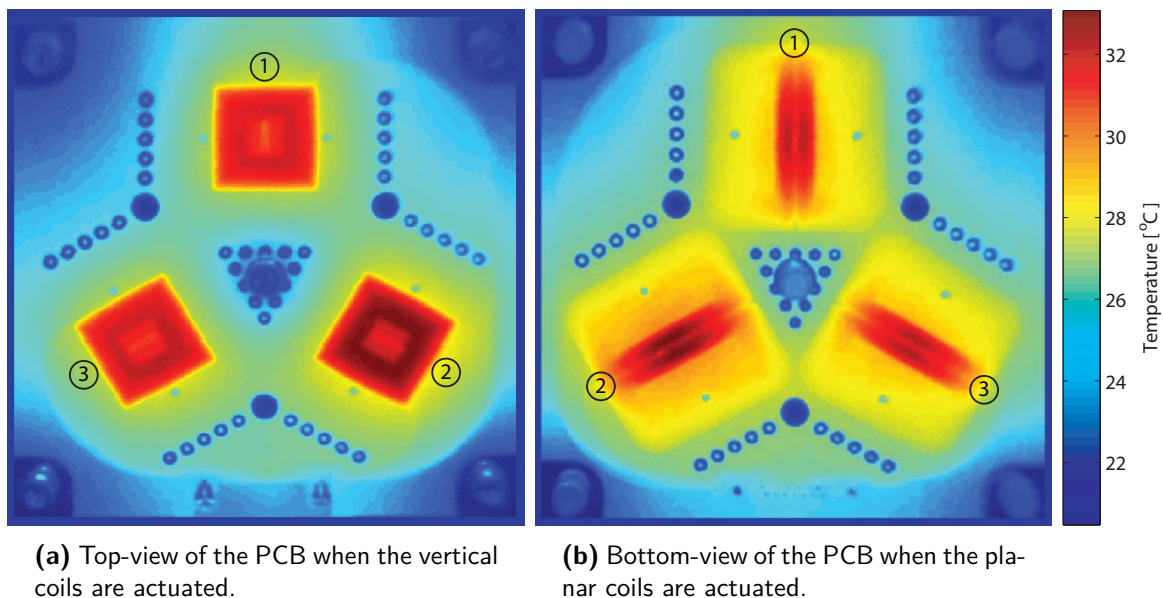


Figure 3.10: Steady state thermal images of the PCB after exposing the coils with a current of 1 A. In both cases the temperature stays well below the required temperature of 80°C.

In Figure 3.11 the temperature at the centre of the coils is plotted over a period of 20 minutes. The thermal time constants of the vertical coils and the planar coils are both roughly 60

seconds. These large thermal time constants make the PCB suitable for short-period high-power inputs.

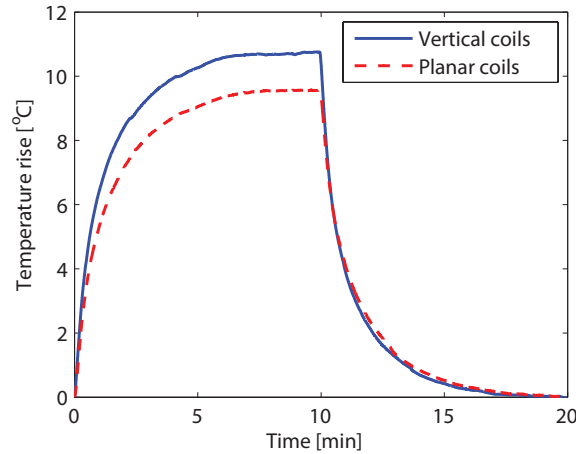


Figure 3.11: Measurement of the average temperature of centre of the coils during 10 minutes of heating them with 1 A. This corresponds to 1.1 Watt per coil for the vertical coils and 1.2 Watt for the planar coils. The thermal time constant τ (of the PCB + aluminium support frame) is roughly 1 minute.

3.8 PCB's dynamic deformation

The PCB is mounted to an aluminium support frame at all four edges and at its centre position. A force between the PCB and the stage can trigger the natural frequencies of the PCB. These eigenmodes will have a negative influence on the achievable bandwidth of the vertical motion. In order to ensure a stable system, the first eigenmode of the system must be significantly higher than the system's bandwidth.

The modal behaviour of the PCB was modelled in COMSOL. The following assumptions were made:

- Since the copper layers add up to a total of less than 7% of the full PCB height, the body is fully modelled as FR4 circuit board, which has a Young's modulus of 22 GPa. The copper layers will make the body stiffer, so the actual system will have a slightly higher eigenfrequency.
- At the screw mounts all movements are fully constrained to zero.

The first eigenmode of the PCB is calculated to be around 420 Hz (Figure 3.12), which is far above the required vertical bandwidth of 43 Hz, so this will not give rise to control problems.

The dynamic deformation of the moving stage also influences the bandwidth of the system. The corresponding modal analysis of the moving stage will be discussed in Section 4.3.

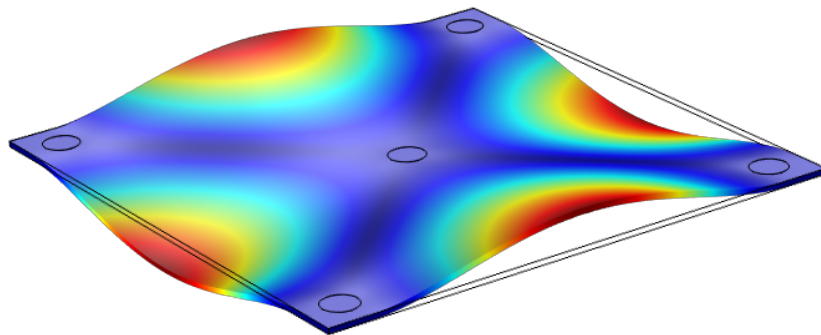


Figure 3.12: The first eigenmode of the PCB is calculated to be around 420 Hz.

Chapter 4

Moving stage

Possible microscopic samples can be placed on top of the moving stage. The bottom-side of this stage (see Figure 4.1) consists of:

- Three magnets which contain the ferrofluid.
- Three interferometry mirrors.
- A support structure, made of PMMA (PolyMethyl MethAcrylate, a transparent thermoplastic).
- A steel top-plate, which is used as a target for the capacitive sensors and a flux-path to increase the efficiency of the magnets.

On each magnet 0.2 ml (APG 12N) ferrofluid is applied. This results in a nominal height of the demonstrator stage z_n of approximately 80 μm . Since the capacitive sensors have a range of 50 μm , they can therefore measure the height of the stage from 55 – 105 μm .

In this chapter the different parts of the stage are discussed and the dynamic response of the stage is investigated.

4.1 Description of individual components

4.1.1 Iron top-plate

The top plate has three purposes:

- **Subsurface.** The potential microscopic sample can be placed on top of the iron plate.
- **Magnetic flux guide.** When the top plate is made of a ferromagnetic material, a flux path for the magnetic field is created, thereby increasing the force of the actuators. More information about this phenomenon can be found in Appendix C. It also provides some magnetic shielding for the components on top of the moving stage.

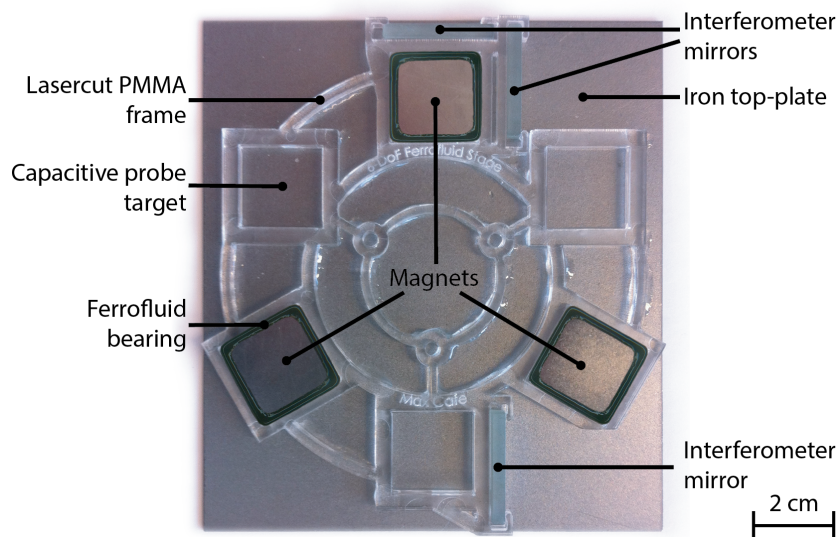


Figure 4.1: Bottom-view of the moving stage.

- **Capacitive probe target material.** The ADE 2805 capacitive sensors use the top plate as their probe target. These sensors will be discussed in Section 5.1. The resistance of the target must be less than $100\text{k}\Omega$ to acquire an RC-time that is sufficiently low.

The dimensions of this steel top plate are $117 \times 105 \times 1$ mm.

4.1.2 PMMA frame

The frame of the stage is made of 4mm thick laser-cut PMMA. Some remarks about the the production process can be found in Appendix G. The difference in the coefficients of thermal expansion (α) between the PMMA and steel can cause additional stresses in the stage. However, the influence of this phenomenon is neglected since the expected temperature rise is sufficiently low. In Figure 4.2 the different elements of the frame are highlighted. Each part is discussed in the paragraphs below:

Magnet mounting The 20×20 mm magnets need to have a spacing of 40 mm from the centre of the stage with an angle of 120° between them, as was stated in Section 3.5. The outlines of the magnets are incorporated in the support frame to position and hold the magnets at the correct location.

Mirror mounting Three plane mirrors reflect the light of the laser interferometers. These mirrors are 25 mm long and 3.3 mm thick. The mirror-mountings clamp those mirrors to the frame. Further information about the interferometers can be found in Section 5.2.

6-DoF force sensor mounting All forces and torques were measured by a 6-DoF Force sensor (see Section 3.6.2). For a correct measurement of those forces, the force sensor has

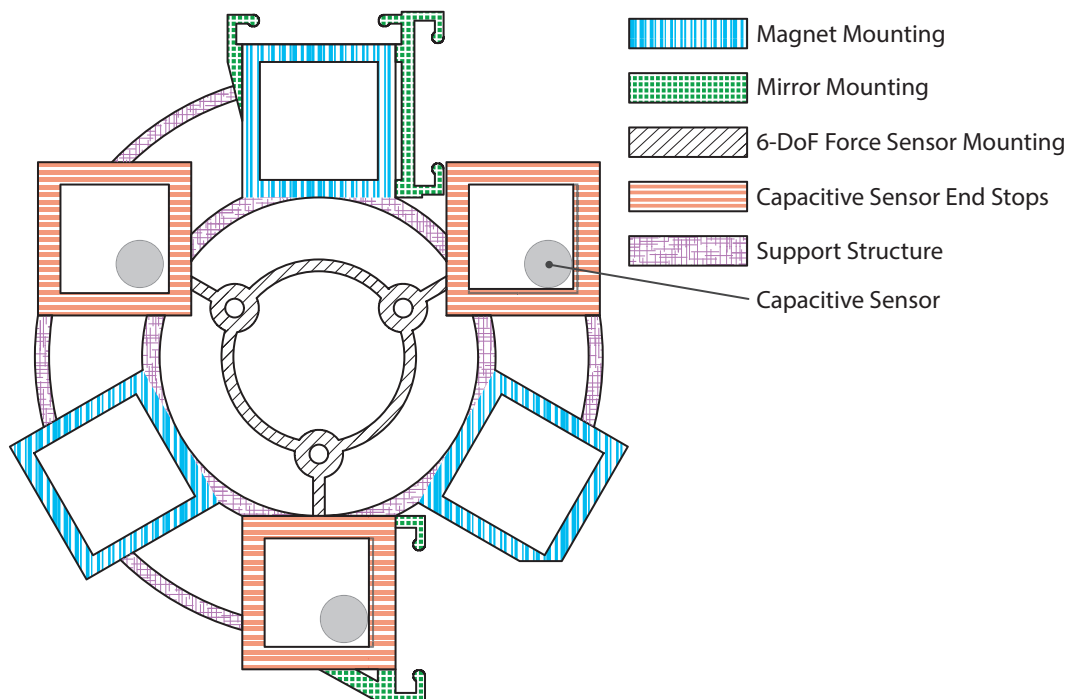


Figure 4.2: The frame of the stage is made of laser-cut PMMA and glued to the steel top-plate.

to be placed at exactly the middle of the stage. The M3 holes of the 6-DoF Force Sensor Mounting indicates the correct position of the force sensor.

Capacitive sensor end-stops The capacitive sensors are placed within the boundaries of the three ‘end-stops’. These end-stops have two purposes:

- **Physically limit the movement of the stage.** Since the ferrofluid bearing has no friction, the stage will move to the lowest location when the actuator is switched off. This can be fully out of range of sensors and actuators. These end-stops will keep the stage within range of the sensors and actuators.
- **Zeroing of the laser interferometers.** The laser interferometers can only measure a relative displacement. To know the absolute value of the displacement these end-stops are used as a fixed reference. At start-up, the actuators exert a force in the x - y -direction until the stage hits the end stops with the capacitive sensors. Since the location of the end-stops is known, the position of the stage relative to the coordinate system can be calculated. The dimensions of the end-stops are such that the system is statically determinate.

Support Structure The support structure keeps all objects at their correct locations and provides additional stiffness to the design.

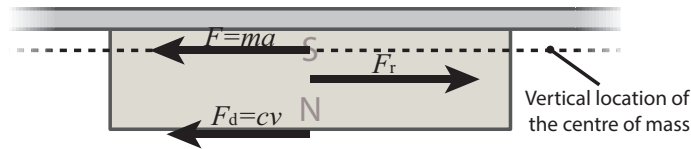


Figure 4.3: Free-body diagram of the forces on the moving stage, where F_r is the resultant actuator force and F_d the damping force. For an application that the stage will mainly stay at fixed positions ($v \approx 0$) and the controller only applies forces for disturbance rejection, it is desired that the vertical centre of mass is at the same height as the resultant actuator force F_r .

4.2 Optimal location of the centre of mass

When a current flows through the coils of the PCB, a force is exerted on the permanent magnets of the moving stage. In Appendix D is described that the point of application of the resultant force is roughly at the middle of the permanent magnets.

In order to get exclusive planar translation, the actuator's point of applications should be such that the resultant of all the system forces yields no moments \mathbf{M} , only a non-zero force in the x - and/or y -direction, so $\sum \mathbf{M} = 0$. For an object with no friction or damping, the centre of mass should be at the same vertical position as the resultant force F_r .

The damping force F_d causes the optimal location of the centre of mass to shift downwards. The damping force is dependent on the velocity of the stage. Since the demonstrator stage moves at different velocities, a single optimal location of the centre of mass cannot be determined.

The centre of mass of the moving stage is at 4.0 mm from the bottom of the magnets. The free-body-diagram of this situation is shown in Figure 4.3.

Right now, the demonstrator stage is not optimized for certain applications. For an application that the stage will mainly stay at fixed positions and the controller only applies forces for disturbance rejection, it is desired to modify the design of the stage such that the vertical centre of mass is at the same height as the resultant actuator force F_r .

4.3 Dynamic deformation

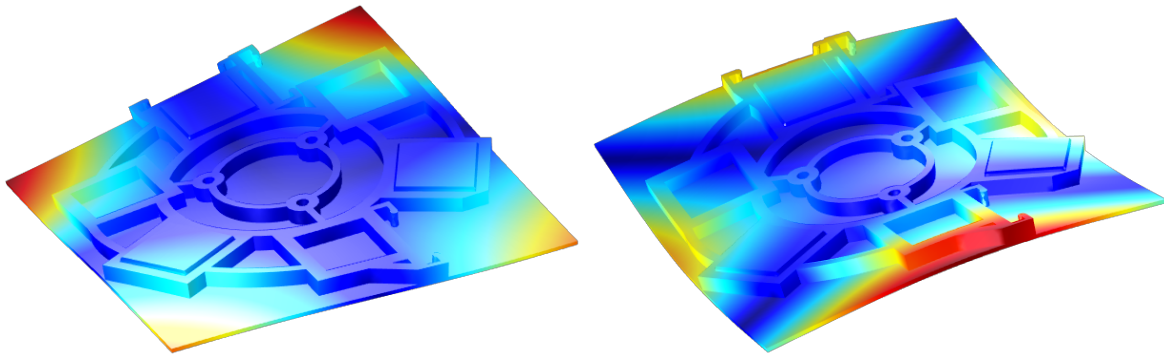
The eigenmodes of the moving stage will have an influence on the achievable bandwidth of the vertical motion. In Section 3.8 was discussed that the first eigenmode of the PCB is sufficiently high, but to ensure a stable system, the first eigenmode of the stage must also be sufficiently higher than the system's bandwidth.

The modal behaviour of the stage was modelled in COMSOL. The following assumptions were made:

- PMMA and the steel plate are fully glued together. The Young's moduli of steel and PMMA are 205GPa and 3GPa respectively. The glue layer has a modelled thickness of 0.1 mm and a Young's modulus of 0.5 GPa.

- The magnets and mirrors can ‘freely’ move and barely have an influence on the stiffness of the stage, only on the mass.

In Figure 4.4 the first two eigenmodes of the stage are shown. The first natural frequency is approximately 280 Hz. The PMMA frame only has a small influence on this natural frequency, since the first natural frequency of only the steel top-plate is 270 Hz. This first eigenmode is roughly 6 times higher than the required bandwidth of 43 Hz, so this will not introduce any control problems.



(a) Stage first eigenmode: approx. 280 Hz.

(b) Stage second eigenmode: approx. 370 Hz.

Figure 4.4: COMSOL model of the first two eigenmodes of the stage. The first eigenmode is roughly 6x higher than the required vertical bandwidth of 43 Hz, so this will not introduce control problems.

Sensors configuration

A capacitive/interferometric measurement system is used for position feedback. The capacitive sensors provide position information about the three vertical DoF: z , θ_x and θ_y . Three laser interferometers provide position information about the planar DoF: x , y and θ_z . The measurement set-up is shown in Figure 5.1. In this picture the actuator PCB is also clearly visible.

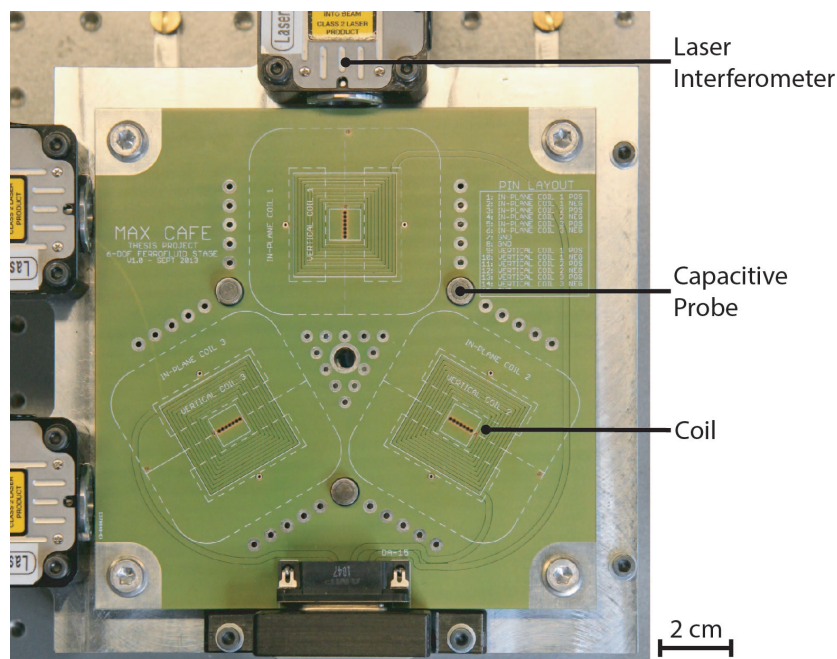


Figure 5.1: Capacitive and interferometric measurement systems, together with the PCB of the demonstrator stage.

5.1 Capacitive sensors

The translation along the z -axis and rotation around the x - and y -axes are measured by three (2805 series) capacitive sensors from ADE Technologies. Each probe has a 5-mm diameter active sensing area and its outer diameter is 8 mm.

The sensor probes are targeted to the bottom of the moving stage. A thin wire is connected from the stage to the chassis to provide electrical ground. The sensor range is 50 μm , which is sufficient to meet the required vertical motion of 25 μm .

An ADE 4800 electronic board converts the probe-to-target distance to a voltage signal of ± 10.0 V. The controller has a 16 bit A-D converter, this comes down to a maximum theoretical resolution R_{cap} of:

$$R_{\text{cap}} = \frac{50 \mu\text{m}}{2^{16} - 1 \text{ counts}} = 0.76 \text{ nm/count} \quad (5.1)$$

The noise level of the capacitive sensors is measured to have a 3σ value of 2.54 nm, this includes the noise caused by the A/D-converters. The Cumulative Power Spectrum (CPS) and Cumulative Amplitude Spectrum (CAS) of this noise is displayed in Figure 5.2. The CAS is defined as the square root of the CPS. The root-mean-square (RMS) noise of the voltage signal $v_{n,\text{RMS}}$ up to 1 kHz is 0.032 mV, which corresponds to 0.08 nm.

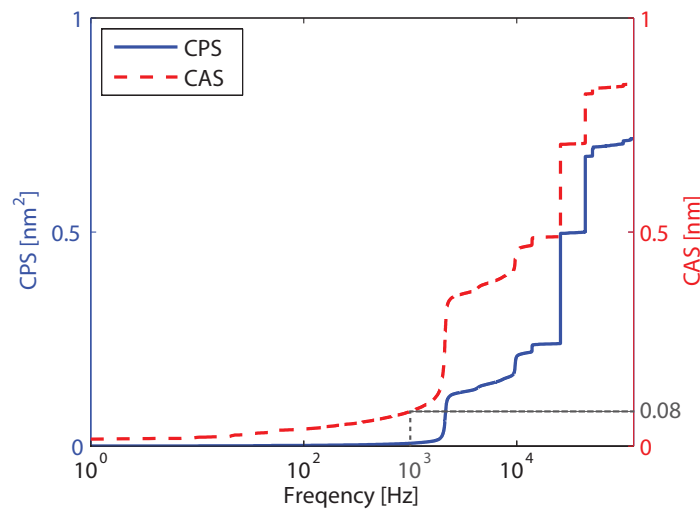


Figure 5.2: Cumulative Power Spectrum (CPS) and Cumulative Amplitude Spectrum (CAS) of the capacitive sensor noise. The root-mean-square (RMS) of the noise voltage signal, $v_{n,\text{RMS}}$ at 1 kHz is 0.032 mV, which equals 0.08 nm.

5.2 Laser interferometers

Position information about the translation along the x - and y -axes and rotation around the z -axis is provided by three (RLE10) laser interferometers from Renishaw.

The 633 nm Helium-Neon lasers have a double pass plane mirror configuration, which directly produces a sinusoidal output with a signal period of 158 nm. This signal is internally converted

to a digital quadrature with a resolution R_{laser} of 10 nm per count. This results in a maximum resolution in the y -direction of 10 nm. The x -position is calculated by taking the mean value of two interferometers (see sensor transformation matrix of Equation A.3), so steps of 5 nm can also be distinguished when the system also has a small rotation around z .

This digital position signal is read out by the digital incremental encoders of the dSPACE 1103 system. Their input frequency is 1.65 MHz, i.e. a fourfold pulse counts up to 6.6 MHz, which results in a maximum velocity of 66 mm/s. This is sufficiently high, so this will not cause any problems for the demonstrator stage.

One of the characteristics of the laser interferometers is that they only give a relative displacement. To obtain absolute position data, it is necessary to use an additional ‘zeroing’. Therefore during the start-up procedure the stage moves to the physical end-stops to define the ‘zero’. These end-stops were discussed in more detail in Section 4.1.2.

5.3 Complete sensor system

The inputs from all six sensors are transformed with a sensor transformation matrix Ψ to the Cartesian coordinate system \mathbf{X} . More information about this matrix can be found in Appendix A.1.

A custom-made aluminium support frame provides a stiff mounting for the sensors and the PCB. It also acts as a large heat-sink for the PCB. The frame is not ferromagnetic, so this will not introduce reluctance forces to the moving stage. Also the influence of eddy-current damping is minimal, since the velocities of the stage are low.

A visualisation of the full system is shown in Figure 5.3. In this visualisation the steel top plate is made transparent, so the underlying components are revealed.

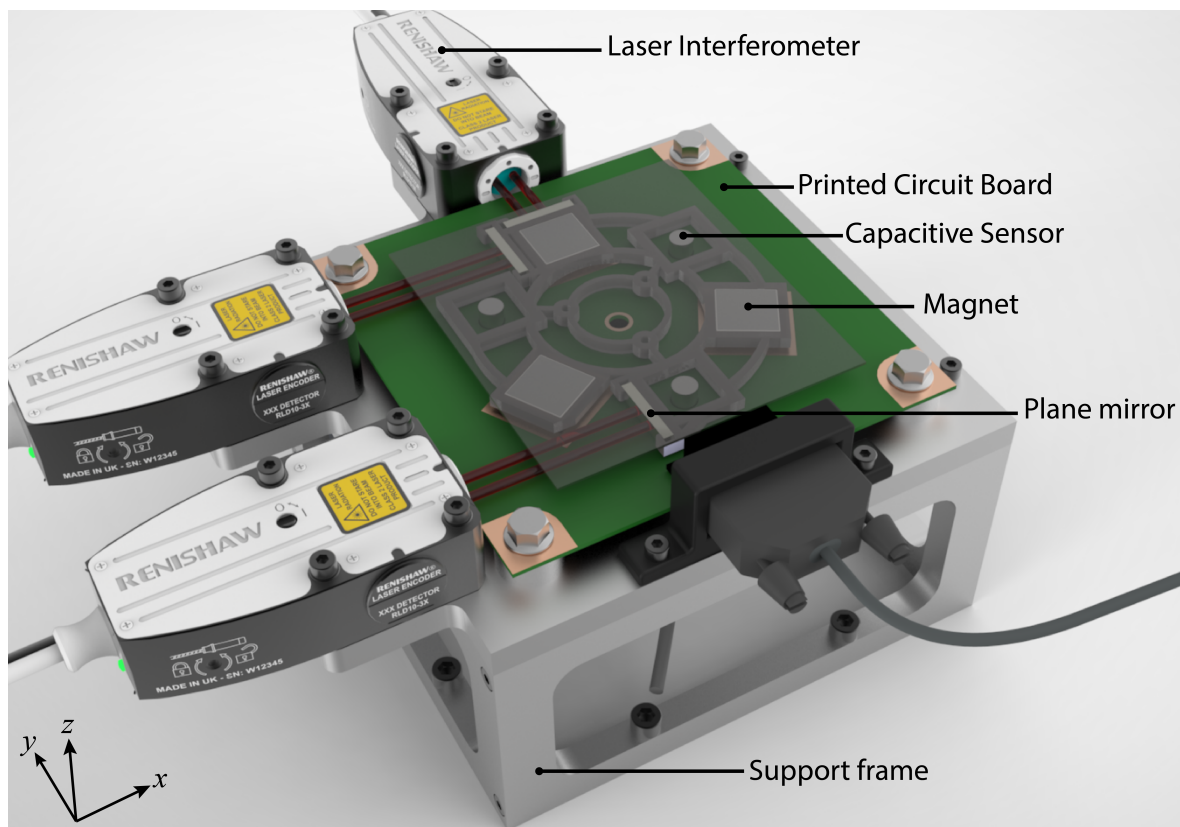


Figure 5.3: Visualisation of the support frame, the PCB, the moving stage and the sensors. The steel top plate is made transparent, so the underlying components are revealed.

Current amplifiers

A Power OpAmp (Operational Amplifier) forms the bridge between the low-voltage, low-current output from the DAC and the (higher) current and voltage signals that are required for the actuators.

The Lorentz coils are an inductive load, so feedback current amplifiers are required to drive these loads with a flat (input to force) frequency response. Custom-made amplifiers were designed and manufactured of which the gain and current-limit can be altered easily.

This section describes the lay-out of those current amplifiers, including the modelling and verification of their performance.

6.1 Schematic of the current amplifier

The OpAmp used in the designed current amplifier is the OPA548 from Texas Instruments. The OPA548 is a low-cost, high-voltage/high-current operational amplifier. It is ideal for driving a wide variety of loads.

A non-inverting current amplifier is built based on the schematic of Figure 6.1a. The gain of the amplifier is given by:

$$\frac{I_o}{V_i} = \frac{R_2}{(R_1 + R_2) \cdot R_3} \quad (6.1)$$

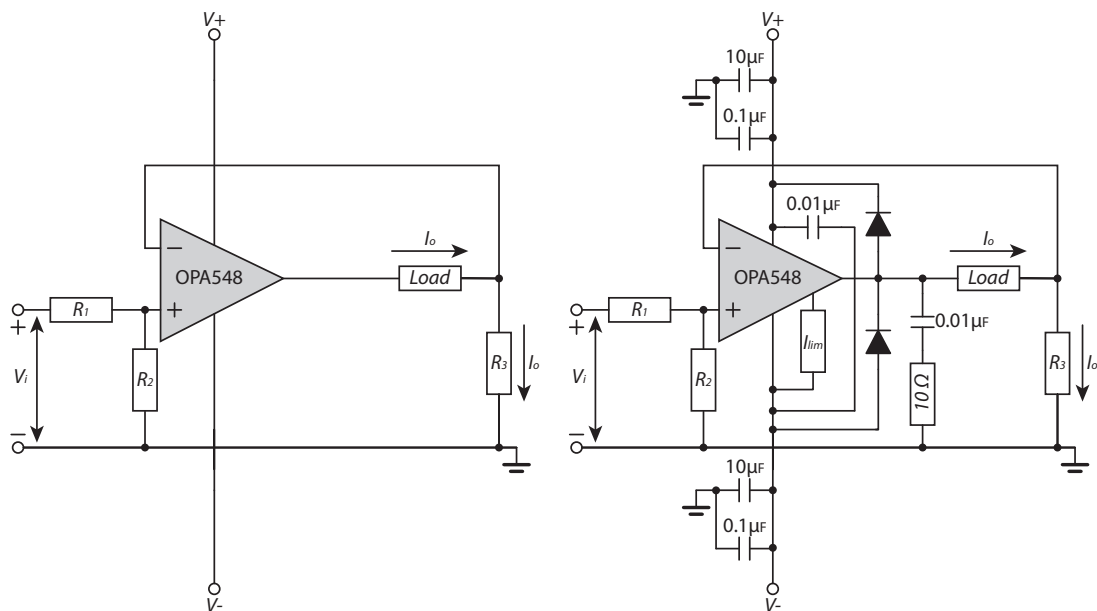
with I_o the output current and V_i the input voltage over the terminals. The voltage divider $\frac{R_2}{R_1+R_2}$ is placed prior to the OpAmp, because when gain of the amplifier is changed, this will not affect the overall frequency behaviour of the amplifier.

The voltage drop over resistor R_3 is directly proportional with the current through R_3 . This voltage drop is therefore used to measure the current output of the amplifier.

In Figure 6.1b the full schematic of the current amplifier is shown. The following additional components are present:

- **Low series impedance capacitors.** The power-supply terminals are bypassed with low series impedance capacitors to get rid of the power-supply noise, as was recommended by Texas Instruments.

- **R/C compensation (snubber) network.** The complex load impedances of the actuator coils may cause output stage instability. Therefore an output series R/C compensation (snubber) network is connected ($10\ \Omega$ and $0.01\ \mu\text{F}$) in parallel with the load.
- **Diodes.** Reactive and EMF-generating loads can return load currents to the amplifier, causing the output voltage to exceed the power-supply voltage. This damaging condition is avoided with the clamp diodes from the output terminal to the power supplies.
- **Current Limiter.** The OPA548 has the advantage over some other OpAmps that the current limit set point is determined by an external resistor that is connected between the I_{lim} -pin and V^- .



(a) Simple schematic with the main components of the current amplifiers.

(b) The full schematic of the current amplifiers. The additional components decrease the noise and make the amplifier more robust.

Figure 6.1: Schematic of the current amplifiers which are used to drive the coils of the Lorentz actuators.

6.2 Performance

The current amplifiers are capable of delivering a continuous output-current of 3 A and a peak output-current of 5 A.

The behaviour of the amplifier in combination with the PCB-coils is simulated using SPICE, an analog electronic circuit simulator. The frequency response of this simulation, together with actual measurements up to 30 kHz are shown in Figure 6.2.

The controller has a cycling frequency of 25 kHz (see Section 7.1), the measurements show up to this frequency a flat gain-line and a phase lag of less than 5 degrees.

An operational amplifier contains many transistors to control the internal currents and voltages. The inclusion of those transistors results in parasitic capacitances. Since the coils are an inductive load, an LC-network arises, which results in a resonance frequency at 200 kHz, accompanied with a phase drop of 180°.

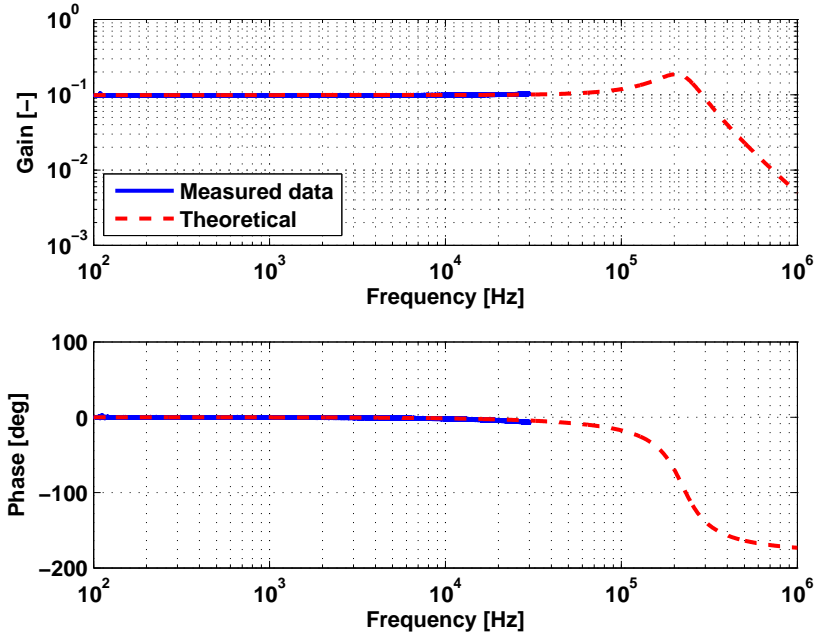


Figure 6.2: Frequency response of the current amplifiers while connected to the PCB coils. The controller has a cycling frequency of 25 kHz (see Section 7.1), the measurements show up to this frequency a flat gain-line and a phase lag of less than 5 degrees.

Noise Level

The cumulative power spectrum (CPS) of the noise is displayed in Figure 6.4a. Up to 1kHz the RMS current noise $I_{n,rms}$ is 0.026 mA.

To get an insight in how much this noise affects the performance and thereby the position of the demonstrator stage, it is necessary to investigate this noise I_{noise} within the closed loop:

$$\frac{y}{I_{noise}} = k_t \frac{G(s)}{1 + C(s)G(s)} \quad (6.2)$$

with $G(s)$ the model of the plant, $C(s)$ the model of the controller and k_t the motor constant. A schematic representation is given in Figure 6.3.

The motor constant k_t is determined by taking the total motor constant in the z -direction, so:

$$k_t = 3k_{t,vert} = 1.2 \text{ N/A} \quad (6.3)$$

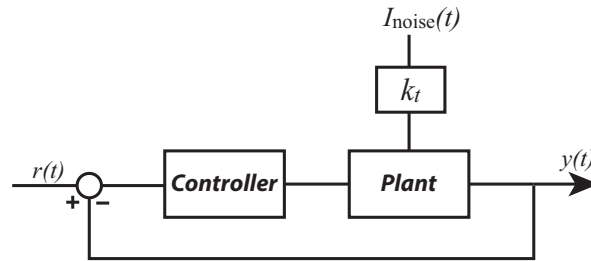


Figure 6.3: The current amplifier noise I_{noise} introduces additional forces on the demonstrator stage, which can cause position errors.

For now, we model $G(s)$ as:

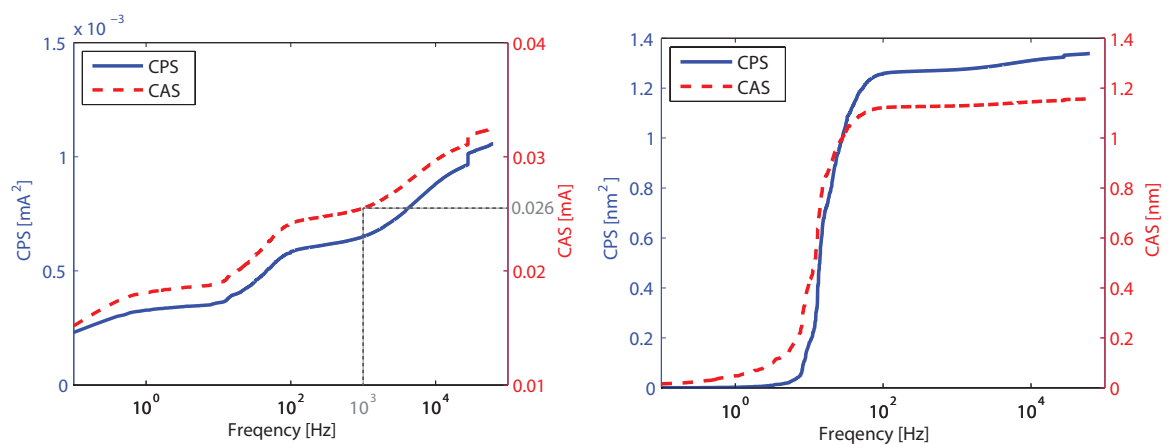
$$G(s) = \frac{1}{ms^2 + cs} \quad (6.4)$$

with m the mass of the stage: 0.15 kg and c the damping. Both the mass as the damper act as a large low-pass filter for the amplifier noise. However, since this damping is unknown, in the next calculations c is set to 0 in order to get an estimate of the worst case scenario.

The controller $C(s)$ is a simple PID controller, more information about PID control can be found in Section 7.3. The controller is tuned to the required 43 Hz (see Chapter 2), following the rules of thumb as suggested by R. Munnig Schmidt in [22]:

$$k_p = \frac{1}{3}m\omega_{BW}^2 \quad k_i = 60k_p \quad k_d = \frac{3k_p}{\omega_{BW}} \quad T_f = \frac{1}{3.3}\omega_{BW}$$

The expected cumulative power spectrum (CPS) and cumulative amplitude spectrum (CAS) of this error are shown in Figure 6.4b. One can see that the expected maximum error, induced by the current amplifier noise, will be just below 1.2 nm.



(a) The cumulative power spectrum (CPS) and the cumulative amplitude spectrum (CAS) of the amplifier noise.

(b) The cumulative amplitude spectrum (CAS) of the expected error ε for the complete system in the vertical direction when the amplifier is connected to the PID controlled stage.

Figure 6.4: The cumulative power spectrum (CPS) and the cumulative amplitude spectrum (CAS) of the amplifier noise in (a) reveals that up to 1kHz the RMS noise level of the current amplifiers is 0.026 mA. In (b) can be seen that this noise results in an expected vertical error ε of the demonstrator stage of approximately 1.2 nm when the damping is neglected and the controller is tuned to the required value of 43 Hz.

6.3 6-in-1 Amplifier assembly

For convenience and robustness of the system, the six current amplifiers are assembled into one amplifier box as can be seen in Figure 6.5. Inside this assembly the output-signals of the individual current amplifiers are conglomaterated into one D-Sub 15 cable. The other end of this cable is connected to the PCB. The pin-out of this cable is listed in Appendix I.



Figure 6.5: The six current amplifiers are assembled into one amplifier box. All output signals are transferred to the PCB via a D-Sub 15 cable.

Control system design

The 6 DoF demonstrator stage is a multiple-input-multiple-output (MIMO) system. The force transformation matrix $\Phi_{\mathbf{F}}(x, y)$ and the sensor transformation matrix Ψ decompose this system into six single-input-single-output (SISO) systems. Six independent PID controllers are used to control the system. A schematic overview of the control-loop is shown in Figure 7.1.

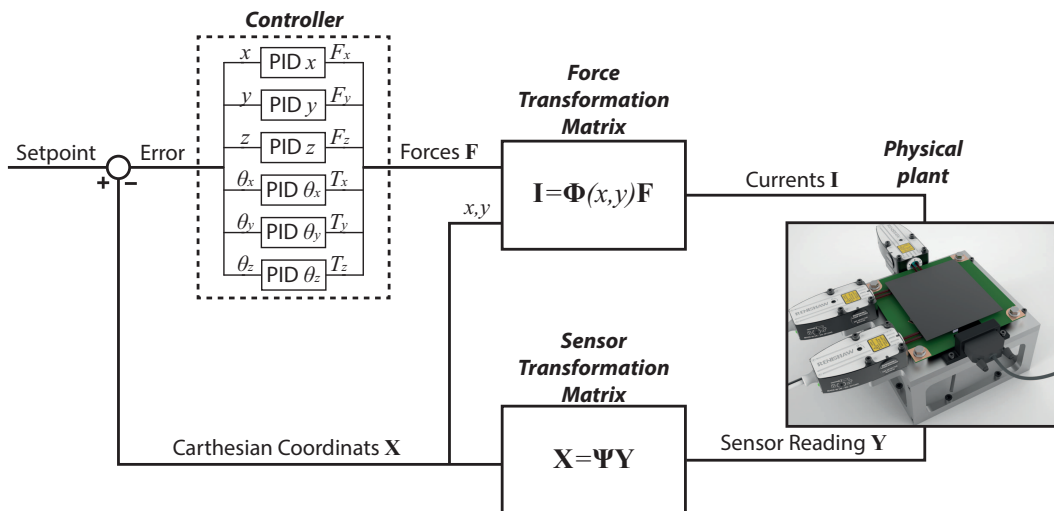


Figure 7.1: Schematic representation of the control scheme.

This chapter describes the design and validation of the controllers.

7.1 Control hardware

The controller is designed in Matlab/Simulink and runs on a dSPACE DS-1103 system. This machine has a 1 GHz processor and 16 bit D/A- and A/D-converters. The full controller runs with a cycling frequency of 25 kHz.

7.2 Performance specifications

The specifications of the controller are related to the open-loop transfer function L :

$$L(j\omega) = CG \quad (7.1)$$

Where C represents the controller and G the plant in the frequency domain.

Before the controller can be designed, first the stability margins must be set. Stability margins allow us to determine the overall stability of the closed-loop system directly from the open-loop design and they also give an indication of the system's stability. Good stability margins can guarantee a certain level of performance and robustness and can prevent uncertainties and perturbations in the system dynamics.

Phase margin φ_m is the amount of phase lag required to reach the stability limit. It is measured as the difference between the phase angle minus 180 degrees when the magnitude of the open-loop transfer function crosses the unity gain.

Gain margin g_m is the amount of loop gain increase before reaching the stability limit. A high gain margin insures that modelling errors in the system gain do not lead to instability. It is measured as the reciprocal of the magnitude when the phase of the open-loop transfer function crosses minus 180 degrees.

Recommended ranges of gain and phase margin are 2 – 5 and $45^\circ - 60^\circ$, respectively [23][24].

The control bandwidth f_{bw} is the lowest frequency where the open-loop transfer function L has a magnitude of 1.

7.3 Introduction to PID control

The control scheme is based on a proportional-integral-derivative controller (PID controller). This control scheme is very intuitive and full knowledge of the underlying process is not required. A PID controller has historically been considered as the best controller when there is no or little knowledge of the underlying process [25].

If $u(t)$ is the control signal sent to the system, $y(t)$ is the measured output and $r(t)$ is the desired output. The tracking error $e(t)$ becomes $r(t) - y(t)$. The general form of a PID controller is:

$$u(t) = K_p e(t) + K_i \int e(t) dt + K_d \frac{d}{dt} e(t) \quad (7.2)$$

The desired closed loop dynamics are obtained by adjusting the three parameters K_p , K_i and K_d .

Differentiation is always sensitive to noise. In a practical controller with derivative action it is therefore necessary to limit the high frequency gain of the derivative term with a first-order derivative filter. This is commonly referred to as a 'tamed' PID controller.

The controller $C(s)$ is the transfer function from measurement output $y(t)$ to the controller output $u(t)$. The transfer function of the ‘tamed’ PID controller is:

$$C(s) = K_p + \frac{K_i}{s} + \frac{K_d s}{\tau_f s + 1} \quad (7.3)$$

where τ_f is the time constant of the first-order derivative filter.

7.4 Planar controllers

System response

The first step of designing a robust controller is getting a good estimate of the frequency response. The frequency response of the system is measured by exciting the system with an input signal, and measuring both input and output time histories. They are compared in the frequency domain by applying a Fast Fourier Transform (FFT) on both signals.

The system response in the x -direction $G_x(j\omega)$ is measured with a frequency sweep from 10 to 3000 Hz. $G_x(j\omega)$ is defined as:

$$G_x(j\omega) = \frac{x_{\text{out}}}{F_{\text{in}}} \quad (7.4)$$

The planar response was measured at $z = 60 \mu\text{m}$, $80 \mu\text{m}$ and $100 \mu\text{m}$, where $z = 80 \mu\text{m}$ is the neutral height of the stage. A gain deviation of around 1.05 was measured from its neutral position. As expected, identical results were obtained for a response in the y -direction.

Since the system will mainly operate at its neutral position of $z \approx 80 \mu\text{m}$, the system is tuned to this vertical position.

The frequency response of the planar system (at $z = 80 \mu\text{m}$) is shown in Figure 7.2a. It can be observed that up to 1000 Hz the system behaves as a pure mass with a -2 slope, but starting from 300 Hz a small phase delay can be observed. This phase delay will be the limiting factor for obtaining a high control bandwidth.

Controller design

A ‘tamed’ PID controller is used to control the system. The following guidelines are used to tune the PID controller:

- The differentiating action (D) is started at one third of the unity-gain cross-over frequency ($0.33\omega_c$) and terminated at $3\omega_c$.
- The integrator action (I) is started at extremely low frequencies and stopped at one third of the starting frequency of the differentiator, approximately $0.1\omega_c$.

The open-loop response $L_{x,y}(j\omega)$ is obtained by multiplying the controller $C_{x,y}(j\omega)$ with the measured system response $G_{x,y}(j\omega)$.

The open-loop gain was increased up to the point that the system still meets the stability margins which were discussed in Section 7.2. The resulting system has a bandwidth of 500 Hz, a phase margin of 45° and a gain margin of 4.

The corresponding controller $C_{x,y}(j\omega)$ and open-loop response $L_{x,y}(j\omega)$ are shown Figure 7.2b-c respectively. The red circles in 7.2c indicate the unity-gain cross-over frequency and the -180° crossing point.

Closed-loop response

The corresponding theoretical closed-loop response $T(j\omega)$ is calculated by:

$$T(j\omega) = \frac{CG}{1 + CG} \quad (7.5)$$

The Bode plot of the closed-loop system is shown Figure 7.2d, where the solid blue line is the theoretical closed-loop response $T_{x,y}(j\omega)$ and the dashed red line the actual response to the system for a reference signal of 100 nm. As expected, they are almost identical. However, a small difference in the phase-response can be observed between the measured and the theoretical closed-loop response. The theoretical closed-loop response decreases earlier in phase and with a slower rate than the measured closed-loop response. A system with low damping has a fast phase drop, this means that the system had a lower damping during the measured closed-loop response than it had during the measurement of the system response $G_x(j\omega)$. The closed-loop response was measured with an amplitude of 100 nm, the system response $G_x(j\omega)$ had an amplitude of >100 nm up to 850 Hz. This means that at the same frequencies the velocities were higher. In [11] was observed that the damping effect became larger with higher velocities, so it is likely that the system also experienced a lower damping during the measured closed-loop response, which explains the different phase characteristics.

Maximum amplitude of the motion

The current amplifiers cannot deliver an infinite amount of current, meaning that at the controller bandwidth f_{bw} (where the closed loop gain drops to below $1/\sqrt{2}$) the system can generate a motion with a maximum amplitude A_{max} :

$$A_{max} = \frac{1}{\sqrt{2}} \cdot \frac{k_t I_{max}}{m(2\pi f_{bw})^2} \quad (7.6)$$

with m the mass of the stage, k_t motor constant of the actuator and I_{max} the maximum current. So for the planar motion this maximum amplitude at a bandwidth f_{bw} of 500 Hz is 1.7 μm .

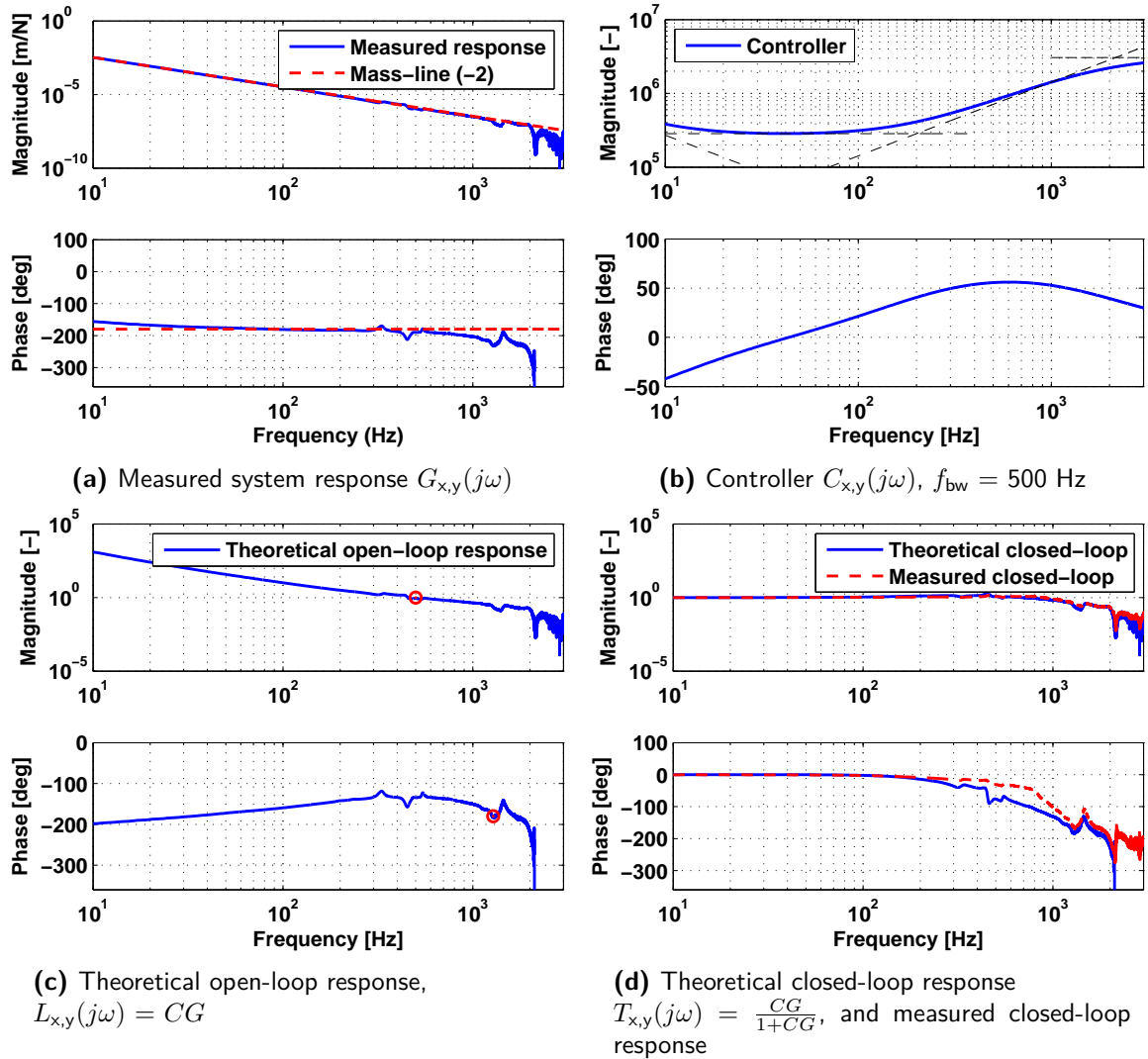


Figure 7.2: The planar motion is controlled with a PID controller, creating a robust system with a bandwidth of $f_{bw} = 500$ Hz. Showing the frequency response of: (a) the system $G_{x,y}$, (b) the tuned PID controller $C_{x,y}$, (c) the resulting theoretical open-loop response $L_{x,y}(j\omega)$, and (d) the corresponding theoretical closed-loop response $T_{x,y}(j\omega)$ (solid blue) and validated closed-loop response (dashed red).

7.5 Vertical controllers

System response

Similar to the planar controller design (Section 7.4), the frequency response of the system is measured firstly.

The frequency response of the vertical motion from 1 to 1000 Hz is shown in Figure 7.3a. The high damping can be observed by both the -1 slope in the magnitude and the corresponding phase, which is roughly -90° up to 100 Hz. At 270 Hz the first resonance peak can be observed and the phase drops below -180° . This resonance peak is caused by the first eigenmode of the stage, which was modelled to be 280 Hz (see Section 4.3).

The measurements were performed at $z = 60 \mu\text{m}$, $80 \mu\text{m}$ and $100 \mu\text{m}$. The neutral height of the stage is at $z \approx 80 \mu\text{m}$. The difference in gain between $z = 60 \mu\text{m}$ and $80 \mu\text{m}$ is 1.25, and the difference between $z = 80 \mu\text{m}$ and $100 \mu\text{m}$ is 1.4. This is quite a large difference, but since the system will mainly operate at its neutral position of $z = 80 \mu\text{m}$, the system is tuned to this height.

Controller design

Due to the high damping of the system, additional D-control is not necessary, so that a PI controller is sufficient.

The integrator action (I) is started at extremely low frequencies and stopped at one tenth of the unity-gain cross-over frequency ($0.1\omega_c$).

In Figure 7.3a can be seen that the resonance peak of 270 Hz has the same amplitude as the system has at 80 Hz. This means that in order to end up with a gain margin of 2, the bandwidth would not be able to exceed 30 Hz. However, a bandwidth of 100 Hz is achieved by adding an additional lowpass-filter to the controller with a cornering frequency at 120 Hz. The controller now has become a ‘tamed’ PI-controller. The corresponding controller $C_z(j\omega)$ and open-loop response $L_z(j\omega)$ are shown Figure 7.3b and 7.3c, respectively. The red circles in 7.3c indicate the unity-gain cross-over frequency and the -180° crossing point.

The system has a phase margin of 55° and a gain margin of 2.

Closed-loop response

The Bode plot of the corresponding closed-loop system is shown Figure 7.2d, where the solid blue line is the theoretical closed-loop response $T_z(j\omega)$ and the dashed red line the actual response to the system for a reference signal of 100 nm. As expected, they are almost identical.

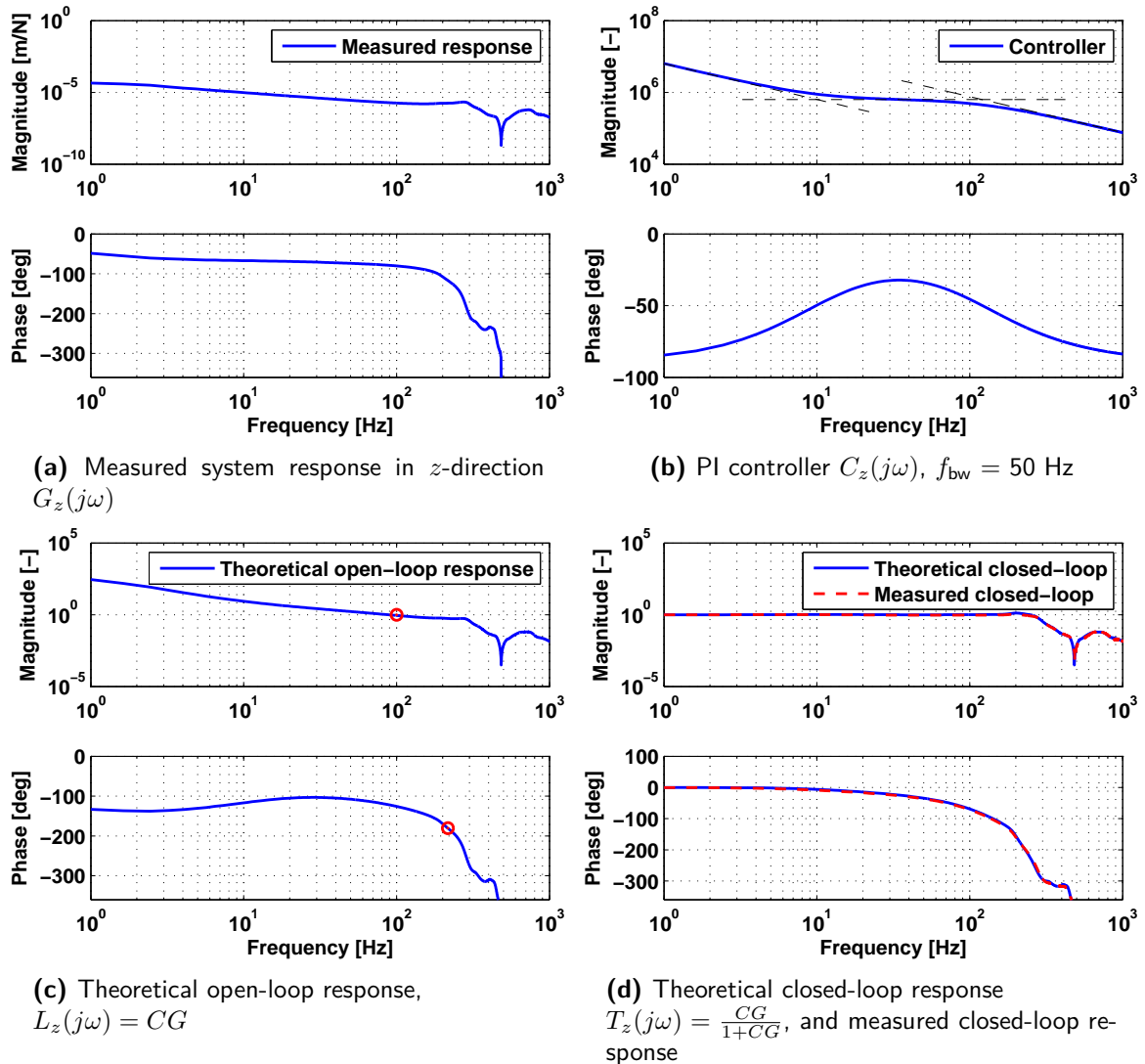


Figure 7.3: The vertical motion is controlled with a tamed PI controller, creating a robust system with a bandwidth of $f_{bw} = 100$ Hz. The figures above show the frequency response of: (a) the system G , (b) the tuned PI controller C , (c) the resulting theoretical open-loop response $L_z(j\omega)$, and (d) the corresponding theoretical closed-loop response $T_z(j\omega)$ (solid blue) and validated closed-loop response (dashed red).

7.6 Additional controller content

7.6.1 Position dependent transformation matrix

In Section 3.6 was discussed that the motor-constant of the actuators is dependent on the position of the stage because the magnetic field moves along with the stage. Also some cross-coupling arises between the actuators when the stage moves to its outer position. It was explained that each position has its own force transformation matrix $\Phi_{\mathbf{F}}(x, y)$ and it was validated that the mean vector error is only 5%. From this model a position dependent lookup-table is extracted for every 100 μm and implemented in the controller. If this lookup-table would not have been implemented, the feedback-loop would have to deal with the position errors that were introduced by the cross-coupling of the coils. Since “*feedback is always too slow*” [22], this would result in higher settling times.

7.6.2 Start-up procedure

At start-up of the system, the absolute planar position of the system is unknown and the stage is possibly out of range of the laser interferometers. Therefore, during start-up the system enters a feed-forward loop that brings the stage to the location of the end-stops. These end-stops were described in Section 4.1.2. When the stage moves to these end-stops, they automatically position the stage within the range of the laser interferometers. Since the location of the end-stops is known, the position of the stage relative to the coordinate system can be calculated.

7.6.3 Safety stop

Without valid position information, the system can become unstable and can thereby damage the set-up. Therefore, the system automatically stops actuating when it recognizes one of the following situations:

- The stage gets out of range of the capacitive sensors.
- The signal strength of the laser interferometers drops below 20%, indicating that the position information is no longer reliable.

7.6.4 Integral anti-windup

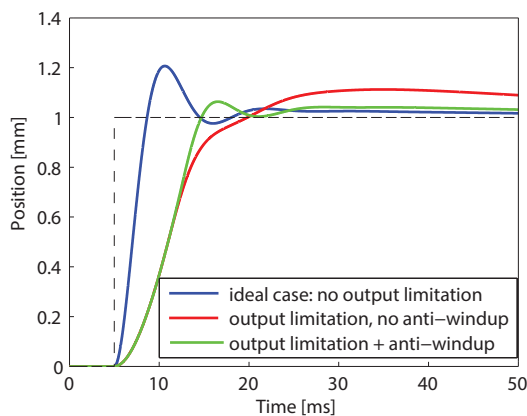
When the actuator output is not high enough to reach the desired setpoint, the error will continue to be integrated and the integrator will grow in size or *wind up*. When the setpoint is changed or when the system finally reaches the desired value, the sign of the error reverses and causes the integrator to *wind down* again. However, the control signal is still maximum during wind down for a certain period of time, causing the response to become delayed. Windup can result in large overshoots, slow settling time and limit cycles.

The goal of the anti-windup scheme is to counteract the integration of the controller when the controller-output exceeds the maximum output of the system. This is performed by feeding the difference between the controller-output and the saturation-limit back to the controller.

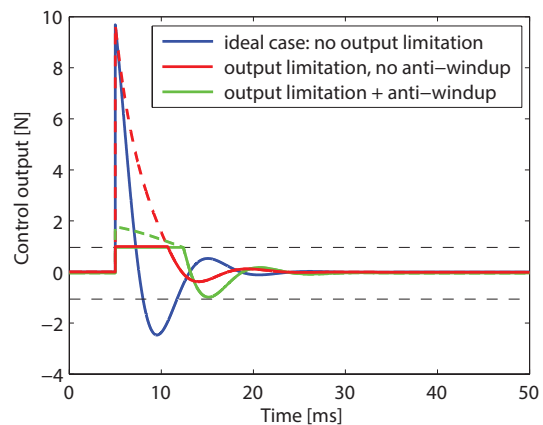
In order to demonstrate the effect of this anti-windup scheme, an example is displayed in Figure 7.4 for the cases where:

- The actuators can deliver an infinite amount of force (blue line).
- The actuators can only deliver a force of 1 N, but no anti-windup measures are taken (red line).
- The actuators can only deliver a force of 1 N, but now the anti-windup scheme is implemented (green line).

The closed-loop step response is displayed in Figure 7.4a and the corresponding control output is displayed in Figure 7.4b. It can be seen that the system with the anti-windup scheme has a faster settling time than without the anti-windup scheme.



(a) Position during closed-loop step response.



(b) Controller output during closed-loop step response.

Figure 7.4: The ideal system has an infinite actuator output, but the actuators of the stage cannot deliver an infinite force. When the system reaches the output saturation, the integration action will continue to increase, resulting in a delayed response and possibly large overshoots and limit cycles. The goal of the anti-windup scheme is to counteract the integration of the controller when the controller-output exceeds the maximum output of the system. This effect is demonstrated for the cases where (1): the actuators can deliver an infinite amount of force (blue line), (2): the actuators can only deliver a force of 1 N, but no anti-windup measures are taken (red line) and (3): the actuators can only deliver a force of 1 N, but now the anti-windup scheme is implemented (green line). It can be seen that the system with the anti-windup scheme has a faster settling time than without it.

Performance measurements

8.1 Stiffness and damping

8.1.1 Vertical stiffness

The relation between the vertical force F_z and the vertical position of the demonstrator stage was measured and plotted in Figure 8.1. It can be observed that within the range of the capacitive sensors (55–105 μm) this relationship is close to linear. The resulting vertical stiffness k_z is 6.5 kN/m. This stiffness is only 50% of the stiffness that was estimated in Section 2.2.2, resulting in a potential increase in vertical range.

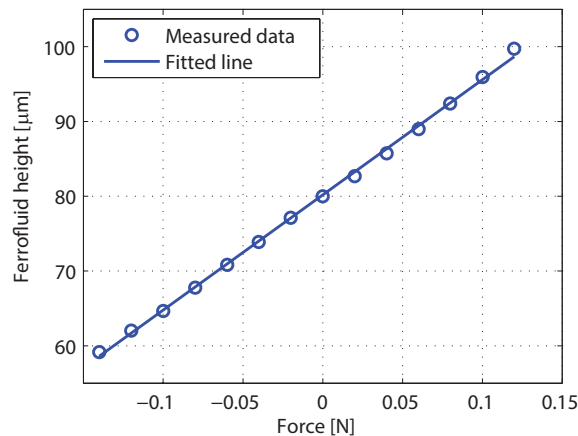


Figure 8.1: Apparent vertical stiffness of the demonstrator stage. Within the range of the capacitive sensors the stiffness curve is close to linear. The resulting stiffness is 6.5 kN/m.

8.1.2 Horizontal and vertical damping

The damping induced by the ferrofluid is non-linear, dependent on the height of the demonstrator stage, the stage's velocity and because of the trail formation also on the history of

the movement. It is observed that for lower locations of z , the damping in both horizontal and vertical direction increases. This is caused by the increased surface area of the ferrofluid. However, the investigation of the full damping of the ferrofluid is beyond the scope of this project and is therefore left open for further research.

8.2 Ferrofluid trail formation

In Section 1.2 was described a stage with ferrofluid bearings leaves some ferrofluid behind during a translational motion, thereby causing the stage to decrease in height. As expected, this decrease in height Δz is highest for the first translational motion. Measurements have shown that Δz can be up to $2 \mu\text{m}$ per mm translation. After a few minutes all ferrofluid is recollected at the magnets, causing the stage to return to its neutral height of $80 \mu\text{m}$.

8.3 Step response

The step response of the system was measured in order to get a good idea of the performance of the demonstrator stage and its overall stability. The reason why a step responses is used, is because a step contains an infinite range of frequencies. In Section 8.1.2 was described that the damping decreases when the height of the stage increases, so it is expected that the settling times will be dependent on the height of the moving stage.

Planar steps

The requirements state that the system must have a settling time (position within $\pm 1\%$ of reference) of less than 0.1 seconds for a planar step of 0.1 mm .

The planar step response is measured for three different heights: its neutral height z_n of $80 \mu\text{m}$ and at $20 \mu\text{m}$ above and below that height. Figure 8.2a shows these three responses. All three responses have a small overshoot, indicating that the system is under-damped. The logical result is that an increased damping will lead to a faster settling time, which is indeed the case: at its nominal height of $80 \mu\text{m}$ the settling time is 19 ms and at $60 \mu\text{m}$ this is 18 ms ; 5% faster. At nominal height the system settles within the sensor resolution of 10 nm of the final value in 32 ms .

At each of the measured locations the system easily meets the requirements. In Table 8.1 the different settling times are listed.

Table 8.1: Settling times of a $100 \mu\text{m}$ planar step.

Height	Settling Time [ms] within $\pm 1\%$ of reference	Percentage of settling time at nominal height [%]
$60 \mu\text{m}$	18	95
$80 \mu\text{m}$ (nominal)	19	100
$100 \mu\text{m}$	20	105

Vertical steps

The requirements state that the system must have a vertical settling time (position within $\pm 1\%$ of reference) of less than 0.1 seconds for vertical steps of 250 nm.

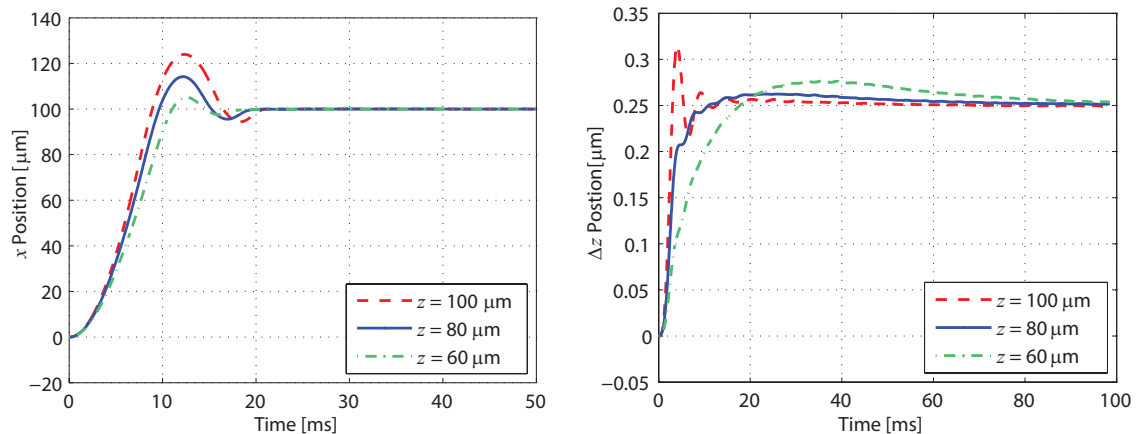
This vertical step response is also measured for three different heights: its nominal height z_n of 80 μm and at 20 μm above and below that height. Figure 8.2b shows these three responses. Again, it can be observed that the damping decreases when the height of the stage increases: the system becomes less-damped and shifts from over-damped to under-damped, thereby decreasing the settling time and increasing the overshoot. The remaining overshoot is caused by the integration action of the controller.

In Table 8.2 the different settling times are listed; at each location the system meets the requirements.

A possible improvement to get rid of for this height-dependent system response, is a (vertical) position-dependent controller. However, due to time limitations, this is not yet implemented.

Table 8.2: Settling times of a 250 nm vertical step.

Height	Settling Time [ms] within $\pm 1\%$ of reference	Percentage of settling time at nominal height [%]
60 μm	85	125
80 μm (nominal)	68	100
100 μm	45	66



(a) Step response in x -direction of 100 μm steps with a control bandwidth of 500 Hz.

(b) Step response in z -direction of 250 nm with a control bandwidth of 100 Hz.

Figure 8.2: Planar (a) and vertical (b) step responses at different heights of the demonstrator stage.

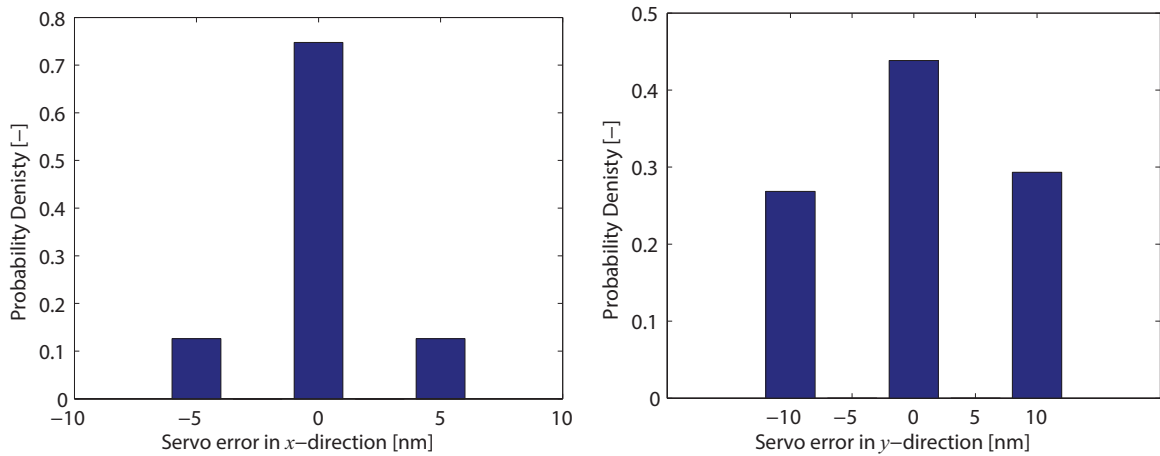
For both the planar as the vertical steps, the settling times are mainly limited by the maximum force of the actuators, because during the first milliseconds the controller-outputs are far higher than the maximum forces that the actuators can produce. When faster settling times are required in future applications, the system can easily be altered to meet those requirement by adding more layers to the PCB and/or increasing the number of windings per layer.

8.4 Positioning precision

8.4.1 Planar precision

The planar position is measured with the laser interferometers. In Section 5.2 was explained that the laser interferometers have a resolution of 10 nm per count. This results in a maximum resolution in the y -direction of 10 nm. The x -position is calculated by taking the mean value of two interferometers (see sensor transformation matrix of Equation A.3), steps of 5 nm can also be distinguished when the system also has some small rotations around z .

Figure 8.3 shows that the demonstrator stage is controlled up to its (effective) sensor resolutions of 5 nm and 10 nm. So right now the precision of the planar motion is fully limited by the sensors. It is expected that the use of sensors with a higher resolution will also increase the precision of the system.



(a) Probability density function of the servo error in the x -direction.

(b) Probability density function of the servo error in the y -direction.

Figure 8.3: Planar precision: The probability density functions of the servo error in x (a) and in y (b) show that the precision of the demonstrator stage is limited by the resolution of the laser interferometers.

8.4.2 Vertical precision

The vertical position is measured with the capacitive sensors. In Figure 8.4a the probability density function of the servo error in z is displayed. It can be observed that the error is normally distributed. The standard deviation of the error is 1.1 nm. The cumulative power spectrum (CPS) of this error is shown in Figure 8.4b. The first two large error sources start at 200 Hz and 700 Hz, which are caused by the eigenfrequencies of the mechanical system. The error at frequencies higher than 2 kHz are mainly caused by the sensor noise. To visualize this, the CPS of the sensor noise is also plotted in Figure 8.3b.

With this high vertical precision, the system is not only suitable for digital microscopy, but also for white light interferometry, where typical steps of half the light's wavelength (250 nm)

are required. White light interferometry is a versatile measurement technology for examining surface topography with very high precision. A more detailed explanation of this technology can be found in Appendix B.2.

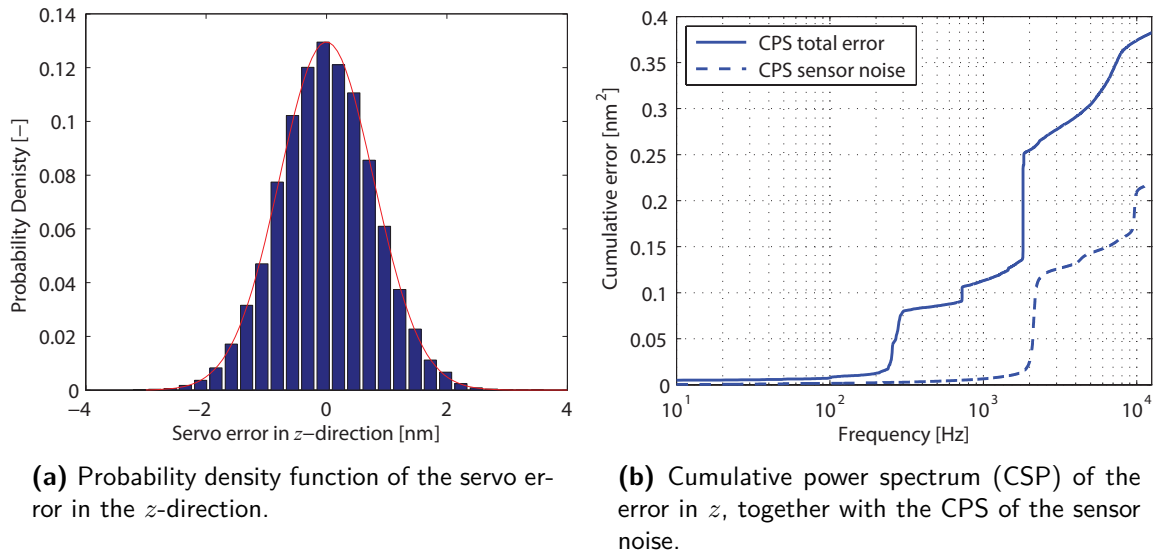


Figure 8.4: Vertical precision: The probability density function of the positioning error in the z -direction (a) shows the standard deviation $\sigma = 1.1$ nm. The cumulative power spectrum of this error (b) shows that the sensor noise is a large contributor to this error at frequencies higher than 1 kHz.

8.5 Specifications of the complete system

Performance (at nominal height):

Planar settling time	19 ms ($\pm 1\%$ of reference)
Vertical settling time	68 ms ($\pm 1\%$ of reference)
Precision in x	5 nm (3σ)
Precision in y	10 nm (3σ)
Precision in z	3.3 nm (3σ)

PCB Actuator:

Resistance vertical coils	1.1 Ω
Resistance planar coils	1.2 Ω
Inductance vertical coils	3.1 μH
Inductance planar coils	4.3 μH
Motor constant planar coils	0.15 N/A
Motor constant vertical coils	0.39 N/A

Sensors:

Capacitive sensor resolution due to ADC	0.76 nm
Laser interferometer resolution	10 nm
RMS noise up to 1kHz of Capacitive sensor	0.032 mV = 0.08 nm
RMS noise up to 1kHz of Laser interferometer	0

Current amplifiers:

RMS noise up to 1 kHz	0.025 mA
Phase delay at 30 kHz	5°
Maximum output current	5 A
Nominal output current	3 A

Physical properties:

Mass moving stage	0.15 kg
Moving stage moment of inertia around x	$1.7 \cdot 10^{-4} \text{ kg} \cdot \text{m}^2$
Moving stage moment of inertia around y	$1.4 \cdot 10^{-4} \text{ kg} \cdot \text{m}^2$
Moving stage moment of inertia around z	$3.0 \cdot 10^{-4} \text{ kg} \cdot \text{m}^2$
Dimensions moving stage	117×105×1 mm
Dimensions PCB:	150×150×1.55 mm

Chapter 9

Conclusions

In this research project a 6 degrees-of-freedom (6 DoF) demonstrator stage with ferrofluid bearings has been built that has a planar precision of 10 nm (3σ) in a range of 10×10 mm, and a vertical precision of 3.3 nm (3σ) in a range of 0.2 mm.

The demonstrator stage is capable of positioning with nanometer precision in x -, y - and z -direction. The ferrofluid bearings do not seem to limit this precision: the planar precision of the demonstrator stage is fully limited by the resolution of the interferometers, where as the vertical precision is mainly limited by the capacitive sensor noise and the mechanical resonances.

The control bandwidth is limited by the mechanical resonances of the PCB and the moving stage. Higher control bandwidths might be achieved when the stiffness of the demonstrator stage is increased.

The forces and torques of the Lorentz actuators are depended on the magnetic field and therefore on the position of the stage (on which the magnets are mounted), also some cross-coupling between the planar and vertical actuators arises when the stage moves to its outer position. These two phenomena are modelled in Matlab and it is verified that this model describes stage's behaviour with 95% accuracy. This model is implemented in the control scheme. The stage also functions properly without this position dependent control scheme, but then the feedback-loop has to cope with the parasitic forces due to the cross-coupling, resulting in increased settling times.

Six current amplifiers deliver the power to the actuators, they show a flat frequency response and a phase lag of only 5 degrees up to 30 kHz. The gain and the current-limit can easily be altered, which makes them suitable for a wide range of other applications.

Although the demonstrator stage is a multiple-input-multiple-output (MIMO) system, a decoupling matrix can break this system down into multiple single-input-single-output (SISO) systems, thereby decreasing the control complexity. For planar translations, the stage shows low damping and very low stiffness, so the system can be treated as a pure mass system, which makes it possible to control it robustly with a simple PID controller. Motions in the vertical direction show much higher damping. Due to this high damping, a PI controller is sufficient for out-of-plane control.

The behaviour of the demonstrator stage is slightly dependent on its vertical position: when the vertical position is increased, the surface area of the ferrofluid is decreased, resulting in a lower damping. Measurements also indicate that the damping increases with higher velocities of the demonstrator stage.

Due to the trail formation of the ferrofluid, the stage can have a decrease in height of up to 2 μm per mm translation. After a few minutes all ferrofluid is recollected at the magnets, causing the stage to return to its neutral height of approximately 80 μm .

Actuation in only 3 DoF can be sufficient when the vertical precision is not very critical. When the vertical DoF are also actuated, the stage can bring (and keep) a microscopic sample in focus of the microscope. With the achieved vertical precision of 3.3 nm (3σ), the system is not only suitable for digital microscopy, but also for white light interferometry, where typical steps of half the light's wavelength (250 nm) are required.

Chapter 10

Recommendations

Some parts were considered to be outside the scope of the project and/or seem valuable for further investigation, therefore some recommendations are listed.

Recommendations considering planar ferrofluid bearings in general:

- More research can be done on the position dependent, non-linear damping of the ferrofluid. This might lead to a model which, when implemented in the control scheme, can lead to an increased performance of roughly 20%.
- The pressure in a magnetized ferrofluid is linearly dependent on the fluid's saturation magnetization. Using a ferrofluid with a higher saturation magnetization can increase the carrying capacity of the bearing.
- The required vertical actuator forces in a ferrofluid bearing system can be decreased when a ferrofluid with a lower viscosity is used.
- For research purposes, very accurate and expensive sensors are used to explore the limits of ferrofluid bearings. For less demanding applications, cheaper and less accurate sensors can be implemented in the system. It is also possible to add them to the same PCB which is used for the Lorentz coils.

Recommendations considering the demonstrator stage:

- The actuator force can be increased by adding additional layers to the PCB. In the current design 4 layers are used while most PCB manufacturers can deliver up to 16 layers.
- In future applications this same PCB can also contain the other electrical components such as the sensors, a digital signal processor (DSP) and potentially also the current amplifiers.
- In the vertical direction, the performance of the demonstrator stage is limited to 100 Hz due to the natural frequencies of both the demonstrator stage and the PCB. If required, this bandwidth can be increased by modifying their design.

- The height-dependent system response might be improved by implementing a vertical position-dependent controller.
- The viscous damping due to the ferrofluid is inversely related to the gap height between the PCB and the stage. In order to reduce damping and hence the step response time, the gap height could be enlarged. This can be achieved by either decreasing the stage mass or by introducing a gravity compensator, such as the placement of repelling permanent magnets beneath the PCB at the stage's magnet locations. This design may also function without any ferrofluid. However in this case the advantages of a stable equilibrium position and damping of vibrations will no longer be present.

Appendix A

Kinematics

A.1 Sensor transformation matrix

The measurement set-up contains three capacitive sensors and three laser interferometers. An overview of the sensor placement was shown in Figure 5.1 of Chapter 5. These sensors are grouped together in the sensor input matrix \mathbf{Y} :

$$\mathbf{Y} = \begin{bmatrix} \text{laser interferometer 1} \\ \text{laser interferometer 2} \\ \text{laser interferometer 3} \\ \text{capacitive sensor 1} \\ \text{capacitive sensor 2} \\ \text{capacitive sensor 3} \end{bmatrix} \quad (\text{A.1})$$

The measurement sensitivity matrix Ψ contains the coordinate transformations between the individual sensor inputs \mathbf{Y} and the trigonometric Cartesian coordinate system $\hat{\mathbf{X}}$. Therefore:

$$\hat{\mathbf{X}} = \Psi \mathbf{Y} \quad (\text{A.2})$$

where Ψ is defined as:

$$\Psi = \begin{bmatrix} 0 & \frac{1}{2} & \frac{1}{2} & 0 & 0 & 0 \\ 1 & 0 & 0 & 0 & 0 & 0 \\ 0 & 0 & 0 & \frac{1}{3} & \frac{1}{3} & \frac{1}{3} \\ 0 & 0 & 0 & \frac{1}{3r} & \frac{1}{3r} & -\frac{1}{1.5r} \\ 0 & 0 & 0 & \frac{1}{r\sqrt{3}} & -\frac{1}{r\sqrt{3}} & 0 \\ 0 & -\frac{1}{2d_{laser}} & \frac{1}{2d_{laser}} & 0 & 0 & 0 \end{bmatrix} \quad (\text{A.3})$$

with r the distance from the centre of the capacitive sensors to the centre of the Cartesian coordinate system and d_{laser} the distance from the centre of the laser beams to the x-axis.

The trigonometric Cartesian coordinate system $\hat{\mathbf{X}}$ is defined as:

$$\hat{\mathbf{X}} = \left[x \quad y \quad z \quad \tan(\theta_x) \quad \tan(\theta_y) \quad \tan(\theta_z) \right]^T \quad (\text{A.4})$$

A.2 Modal force transformation

The modal force transformation converts the forces applied at each of the actuator locations into forces and torques relative to the centre coordinate system:

$$\mathbf{F} = \Phi_{\mathbf{F}} \mathbf{F}_{\text{coils}} \quad (\text{A.5})$$

In symbolic notation, the force transformation matrix is defined as:

$$\Phi_{\mathbf{F}} = \begin{bmatrix} 1 & -\frac{1}{2} & -\frac{1}{2} & 0 & 0 & 0 \\ 0 & -\frac{\sqrt{3}}{2} & \frac{\sqrt{3}}{2} & 0 & 0 & 0 \\ 0 & 0 & 0 & 1 & 1 & 1 \\ 0 & 0 & 0 & r & -\frac{r}{2} & -\frac{r}{2} \\ 0 & 0 & 0 & 0 & -\frac{r\sqrt{3}}{2} & \frac{r\sqrt{3}}{2} \\ -r & -r & -r & 0 & 0 & 0 \end{bmatrix} \quad (\text{A.6})$$

with r the distance from the centre of coils to the centre of the Cartesian coordinate system.

The modal force matrix is:

$$\mathbf{F} = \left[F_x \quad F_y \quad F_z \quad T_x \quad T_y \quad T_z \right]^T \quad (\text{A.7})$$

and the actuator forces are:

$$\mathbf{F}_{\text{coils}} = \left[F_{\text{plane1}} \quad F_{\text{plane2}} \quad F_{\text{plane3}} \quad F_{\text{vert1}} \quad F_{\text{vert2}} \quad F_{\text{vert3}} \right]^T \quad (\text{A.8})$$

$F_{\text{plane1,2,3}}$ are the forces created by in-plane coils 1,2 and 3, $F_{\text{vert1,2,3}}$ are the forces created by vertical coils 1,2 and 3, respectively.

The controller gives the modal force matrix \mathbf{F} as output. It is therefore necessary to use the inverse matrix $\Phi_{\mathbf{F}}^{-1}$ for calculating the actuator forces $\mathbf{F}_{\text{coils}}$ from the modal forces. Symbolically, the inverse matrix is:

$$\Phi_{\mathbf{F}}^{-1} = \begin{bmatrix} \frac{2}{3} & 0 & 0 & 0 & 0 & -\frac{1}{3r} \\ -\frac{1}{3} & -\frac{\sqrt{3}}{3} & 0 & 0 & 0 & -\frac{1}{3r} \\ -\frac{1}{3} & \frac{\sqrt{3}}{3} & 0 & 0 & 0 & -\frac{1}{3r} \\ 0 & 0 & \frac{1}{3} & \frac{2}{3r} & 0 & 0 \\ 0 & 0 & \frac{1}{3} & -\frac{1}{3r} & -\frac{\sqrt{3}}{3r} & 0 \\ 0 & 0 & \frac{1}{3} & -\frac{1}{3r} & \frac{\sqrt{3}}{3r} & 0 \end{bmatrix} \quad (\text{A.9})$$

Appendix B

Additional information

B.1 Digital microscopy

The introduction of motorized XY stages in microscopy has dramatically improved their operability. With this planar movement, the user can now easily make fine position adjustments at any magnification.

In biomedical and clinical studies, it is often highly desirable to observe images of whole tissue sections with high resolution in two or three dimensions. However, those regions are too large to be captured by a single image at a sufficient magnification. Therefore, it is common experimental practice to capture multiple photographic images with overlapping field of view to produce a panorama or larger image with high resolution. This process is commonly referred to as stitching [26].

With image stitching, the view is enlarged and the amount of information increases with the number of images that are stitched. The advantages of stitching are clarified in Table B.1. By stitching together higher magnification 3D images, it is also possible to acquire the depth information over a large field of view.

When the Z axis is also actuated, complex focus adjustments are no longer necessary since autofocus can take over that job.

Table B.1: Image stitching has the advantages of both low and high magnification observations. The green highlighted properties are the desired specifications.

	Low magnification	High magnification	Image stitching
Field of view	Wide	Narrow	Wide
Depth of field	Deep	Shallow	Deep
Resolution	Low	High	High
3D display	Impossible	Possible	Possible

B.2 White light interferometry

Interferometry is a versatile measurement technology for examining surface topography with very high precision. At the heart of interferometry is the interferogram, which is the recorded interference signal of two beams of light originating from the same source. An interferogram carries a wealth of information about the profile of an object under test and its material characteristics; its fringes, like lines on a topographic map, represent the topography of the object [27].

The most popular interferometric measurement techniques are phase-shifting interferometry (PSI), vertical scanning interferometry (VSI), and enhanced VSI (EVSI). A detailed description can be found in for example [28].

For rough surfaces, a white-light VSI approach is effective because the light source is better-suited for the application, and no longer is looked at the shape of the fringes but rather is searched for the best-focus position.

During the measuring process of VSI, the optical path difference is steadily increased by scanning the objective vertically using a precision stage. Interference data are captured at each step in the scan or at the camera frame rate.

Scanning white light interferometry is a technology which combines an interferometer and microscope into one instrument. It is used to provide a non-contact, 3D method of measuring surface profiles.

Illumination from a white light beam passes through a filter and then a microscope objective lens to the sample surface. The objective lens is coupled with a beam splitter such that some of the light is reflected from a reference mirror. The light reflecting back from the surface recombines with the reference beam. The recombined beams create bright and dark bands called fringes, which make up the interferogram. Those fringes represent the object's topography [29].

When the required measurement areas are larger than the field of view, a stitching procedure can be employed that involves a number of partially overlapping measurements being combined into one surface profile.

B.3 Working principle of a Lorentz actuator

The Lorentz Force Law states that the force \mathbf{F} acting on a particle of electric charge q with instantaneous velocity \mathbf{v} , due to an external electric field \mathbf{E} and magnetic field \mathbf{B} , is given by: [30]

$$\mathbf{F} = q(\mathbf{E} + \mathbf{v} \times \mathbf{B}) \quad (\text{B.1})$$

When a wire carrying an electrical current is placed in a magnetic field, each of the moving charges, which comprise the current, experiences a Lorentz force, and together they can create a macroscopic force on the wire. The magnetic force on each charge is $q\mathbf{v}_d \times \mathbf{B}$, where \mathbf{v}_d is the drift velocity of the charge carriers. The number of charges in the wire segments is the number n per unit volume multiplied by the volume $A\ell$. Thus, the total force on the wire segment is

$$\mathbf{F} = (q\mathbf{v} \times \mathbf{B})nA\ell \quad (\text{B.2})$$

The electrical current through a wire is defined as:

$$I = nqv_dA \quad (\text{B.3})$$

By combining the Lorentz force law of Equation B.2 with the definition of electrical current, the following equation results (in the case of a straight, stationary wire):

$$\mathbf{F} = I\boldsymbol{\ell} \times \mathbf{B} \quad (\text{B.4})$$

where \mathbf{B} is again the magnetic flux density, $\boldsymbol{\ell}$ is a vector whose magnitude is the length of wire, and whose direction is along the wire, aligned with the direction of the current flow I . This relation can also be visualised by the ‘‘right hand rule’’ as can be seen in Figure B.1.

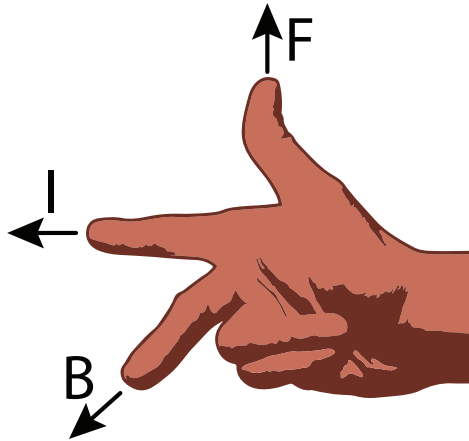
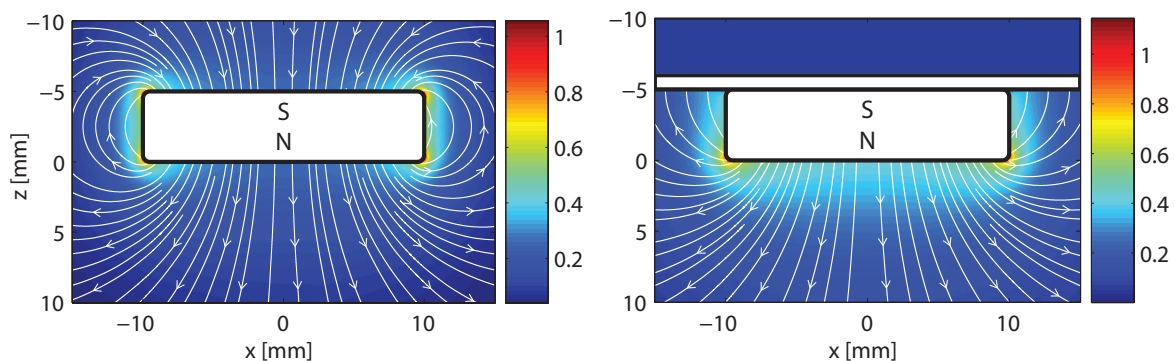


Figure B.1: The force resulting from a current is perpendicular to the magnetic field and the current; the ‘‘right hand rule’’ is an easy way to remember this.

Lorentz (i.e. voice coil) actuators are governed by the Lorentz force principle. They are simple electromechanical devices which generate precise forces in response to an electrical input signal. Because of the linear relationship between force and current, a voice coil actuator can be used for precise force control. The actuator itself is very reliable since no commutation is required for motion to occur.

Influence of an iron plate to the magnetic field

The magnetic field \mathbf{B} can be represented by magnetic field lines. The direction of the field is indicated by the direction of the field lines and the magnitude of the field is indicated by the density of the lines. Figure C.1a shows the magnetic field lines on the outside of the magnet. The strength of the magnetic field below the magnet can be increased by adding an iron plate on top of the magnet as can be seen in Figure C.1b. An increased magnetic field results in an increased actuator force. This principle is therefore used in the design of the moving stage.



(a) Magnetic field lines outside a block magnet

(b) Magnetic field lines outside a block magnet with additional iron plate

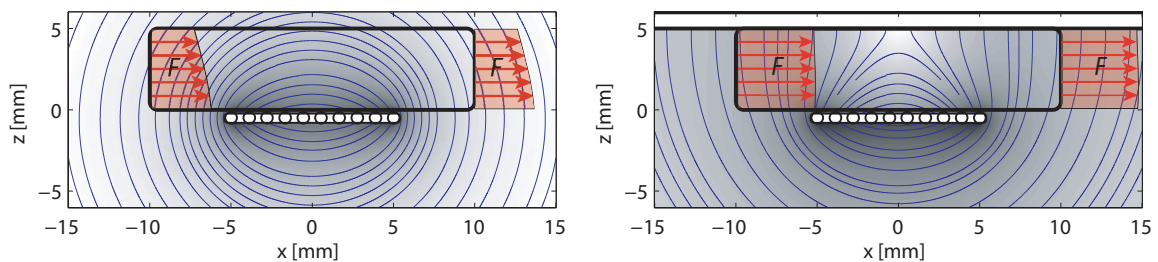
Figure C.1: COMSOL models of the magnetic flux density of a Neodymium permanent magnet in air without a steel top plate (a) and with a steel top plate (b). It can be seen that the magnetic flux density below the magnet is higher with the addition of a steel top plate. The horizontal flux component decreases more rapidly with a greater distance from the magnet than the vertical flux component. It is therefore more essential that wires for the vertical force are closer to the magnet than the wires for the in-plane force.

Resultant force on moving stage

When a current flows through the coils of the PCB, a force is exerted on the permanent magnets of the moving stage.

The magnetic field of the permanent magnets can be replaced by equivalent bound currents. So by integrating the magnetic field over the boundaries of the permanent magnet, the force acting on the stage can be calculated. A more detailed explanation about bound currents can be found in e.g. [21].

The vertical location \bar{z} of the resultant force F_r is influenced by the addition of the steel top plate on top of the magnets. A visualisation of the resultant force on the magnet for a situation with- and without steel top plate is shown in Figure D.1. It can be seen that the location of the resultant force of the demonstrator stage is approximately at half the height of the magnet.



(a) Resultant force induced by the coils without steel top plate.

(b) Resultant force induced by the coils with steel top plate.

Figure D.1: The vertical location of the resultant force \bar{z} is influenced by the addition of the steel top plates to the magnets. A visualisation of the force on the magnets that is induced by the magnetic field of the coils is shown in (a). In (b) this magnet has an additional steel plate on top, causing the point of application of the resultant force to shift upwards.

Appendix E

Modelling the number of windings

To stay in the linear operation area of the Lorentz actuator, all the windings must be underneath the magnet for every position of the stage, this leaves a spacing of 10 mm where the windings can be (see Section 3.1).

Number of Windings

The number of windings n of the coil is dependent on the gap width d_{gap} , the track width d_{track} . The total width of the windings d_{total} is characterized by the following equation:

$$d_{\text{total}} = n \cdot (d_{\text{track}} + d_{\text{gap}}) - d_{\text{gap}} \quad (\text{E.1})$$

so

$$n = \frac{d_{\text{total}} + d_{\text{gap}}}{d_{\text{track}} + d_{\text{gap}}} \quad (\text{E.2})$$

The gap- and track width have both a minimum distance of 150 μm . To maximize the effectiveness force of the Lorentz actuator, a fixed gap width of 150 μm is chosen.

Required Current

The required current I per coil to generate force F_{coil} is:

$$I = \frac{F_{\text{coil}}}{n \cdot B \cdot \ell \cdot k} \quad (\text{E.3})$$

with B the magnetic field, k the number of PCB layers and ℓ is a vector whose magnitude is the length of wire, and whose direction is along the wire, aligned with the direction of the current flow I .

Resistance

The vertical coils are located on PCB layer 1 and 2. The height of layer 1 h_1 is 0.018 mm, the height of layer 2 h_2 is 0.035 mm. The planar coils are located on layers 3 and 4, with the corresponding heights of $h_3 = 0.035$ mm and $h_4 = 0.018$ mm. A schematic representation of the PCB build-up was shown in Figure 3.3 of Section 3.4.

The total resistance of vertical movement coils R_{vert} is approximated by the following formula:

$$R_{\text{vert}} = 4 \cdot \frac{\rho \cdot \ell \cdot n}{d_{\text{track}}} \cdot \left(\frac{1}{h_1} + \frac{1}{h_2} \right) \quad (\text{E.4})$$

with ρ the electrical resistivity of copper ($1.68 \cdot 10^{-8} \Omega\text{m}$).

The planar windings beneath the magnet (the force generating part) are smaller than the windings of the return path. Therefore the resistance of planar movement coils R_{plane} is split into two parts. The resistance of the force generating part is:

$$R_1 = \frac{\rho \cdot l_1 \cdot n}{d_{\text{track}}} \left(\frac{1}{h_3} + \frac{1}{h_4} \right) \quad (\text{E.5})$$

The windings of the return path have a resistance of:

$$R_2 = \left(\frac{\rho \cdot l_1 \cdot n}{d_2} + 2 \cdot \frac{\rho \cdot l_2 \cdot n}{d_2} \right) \left(\frac{1}{h_3} + \frac{1}{h_4} \right) \quad (\text{E.6})$$

with d_2 the width of the windings of the return path. l_1 and l_2 are the average lengths of the windings as is schematically shown in Figure E.1.

The total resistance of a planar coil R_{plane} becomes:

$$R_{\text{plane}} = R_1 + R_2 \quad (\text{E.7})$$

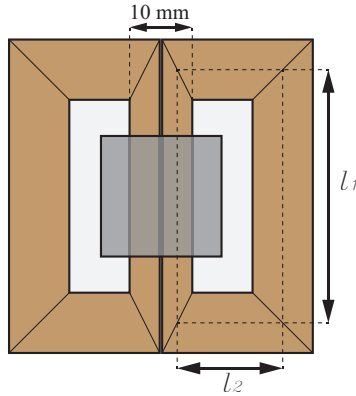


Figure E.1: Representation of the dimensions of the planar coils.

Temperature Rise

The Power dissipated per coil is:

$$Q = I^2 R \quad (\text{E.8})$$

Since there are 3 coils for the planar movement and 3 coils for the vertical movement, the total power dissipated is $3Q$.

From the dissipated power a rough estimation can be made about the total temperature rise dT of the PCB when the assumption is made that all the heat is transferred to the air by means of convection:

$$dT = \frac{3 \cdot Q}{h_{\text{air}} \cdot A_{\text{surface}}} \quad (\text{E.9})$$

With h_{air} the heat transfer coefficient of air: $5 \text{ W/m}^2\text{K}$ and a the total surface area of the PCB.

For a more effective heat transfer to the environment, it is desired to have as much copper as possible in the PCB, since copper has a much higher thermal conductivity than FR4: 400 W/(mK) instead of 0.25 W/(mK) . So therefore A_{surface} is assumed to have the same surface area of the PCB: $150 \times 150 \text{ mm}$. It is also assumed that the total surface of the PCB contributes to the convective surface area.

Appendix F

Planar coil concepts

There are two possible configurations to achieve a low position dependency in the full stroke of the actuator (10 mm):

- Option A: Place the coil windings from -15 to +15 mm, making this coil configuration 30 mm wide, see Figure F.1a. This situation can be compared to an over-hung voice coil.
- Option B: Place the windings from -5 to +5 mm, making this coil configuration 10 mm wide, see Figure F.1b. This situation can be compared to an under-hung voice coil.

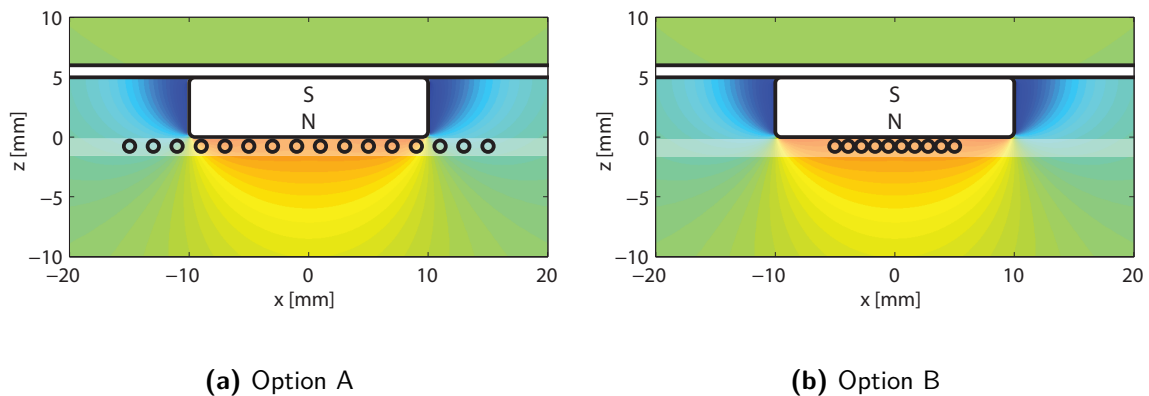


Figure F.1: To achieve a low position dependency in the full stroke of the actuator (10 mm), there are two possible configurations: In option A (a) the coil windings are located from -15 to +15 mm, making this coil configuration 30 mm wide. In option B (b) the windings are located from -5 to +5 mm, making this coil configuration 10 mm wide.

Option A has the advantage that the full vertical field is used. This means the windings can be thicker, which reduces the resistance and thereby the power loss of the PCB. The disadvantage is that the wires from 10 till 15 mm and -10 till -15 mm experience the return path of the magnetic field, thereby negatively contributing to the force. To generate the same force as option B, option A requires roughly 1.7 times the number of windings than option

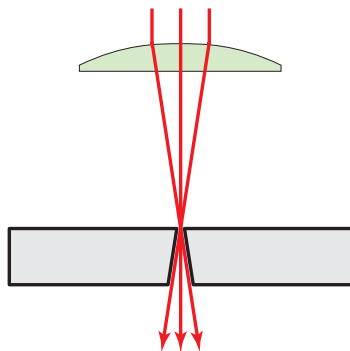
B. Of course all windings also need to return in order to form a closed path, therefore this option requires quite a lot of space on the PCB. This results in a large and therefore more expensive PCB.

Option B uses only 50% of the vertical magnetic field, but the return path of the wires can be placed in the return path of the magnetic field, therefore positively contributing to the Lorentz force.

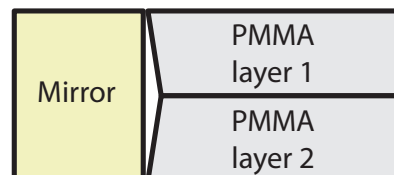
The low price of the PCB has a higher priority than its efficiency, thus in the final design of the planar coils, option B is chosen.

Production of the stage's frame

Initially, the frame was laser-cut out of a 4 mm thick PMMA plate. However, this gave a problem with the alignment of the laser interferometer mirrors: The laser beam is focused at an angle to a spot, so no cut can be perfectly square as can be seen in Figure G.1a. This caused a severe misalignment of the laser interferometer mirrors, so no planar position data could be achieved. This problem was solved by glueing two mirrored 2 mm PMMA plates together, see Figure G.1b.



(a) Schematic of a laser cut.



(b) Two mirrored layers of PMMA provide a parallel mounting for the laser interferometer mirrors.

Figure G.1: A schematic of a typical laser cut is shown in (a): the laser beams are focussed on the top surface of the object, resulting in a non-squared cut. When the mirrors are not mounted parallel to the laser interferometer-beams, the reflected light does not reach the sensor. Therefore the frame is made out of two stacked layers of PMMA, resulting in a parallel mount for the mirrors.

Appendix H

1-DoF Ferrofluid stage

A 1-DoF linear ferrofluid stage was designed by Van Veen [15] on which a precision of 10 nm (σ) was reached. This stage was improved to a precision of 1.6 nm (σ).

H.1 Original 1-DoF stage

The linear stage was firstly built with a 4.88 nm-resolution encoder, an Arduino Uno micro-controller and PWM current amplifier with a PID feedback controller. The stage is actuated by a Lorentz actuator with a strength of 0.63 N/A. A control bandwidth of 100 Hz was achieved. The stage was positioned with a precision of 10 nm over a range of 20 mm.

H.2 Improved 1-DoF stage

The 1-DoF stage was altered to reach a higher precision with the components that were readily available in the lab.

The calculations are done by an Arduino Due micro-controller board. This micro-controller is 5.25 times faster than the Arduino Uno used by Van Veen. An additional capacitive sensor is added in line with the Lorentz actuator to reach a higher precision. The sensor's analog signal is converted to the digital domain by an A/D converter. The PWM current amplifier is replaced by a D/A converter and a custom build current amplifier. The differences are listed in Table H.1.

Table H.1: Comparison between old and enhanced 1-DoF setup

	Old Setup	Enhanced Setup
Micro-Controller	Arduino Uno (16 MHz)	Arduino Due (84 MHz)
Sensor	Linear Encoder (4.88 nm res.)	Linear Encoder (4.88 nm res.) Capacitive Sensor (0.7 nm res.)
Amplifier	8 Bit PWM current amplifier	16 Bit analog current amplifier
Actuator	Lorentz actuator	Lorentz actuator

Capacitive Sensor

A 2805 series capacitive sensor probe from ADE technologies was placed in line with the actuator, thereby eliminating the Abbe error. Further reading on the capacitive sensor can be found in Section 5.1.

D/A and A/D Converters

DAC ports of the Arduino Due The Arduino Due has two build-in 12-bit DAC ports. These DAC-ports are not used to control the current amplifier because it does not vary between the desired ± 10 Volt range, but between $1/6^{\text{th}}$ and $5/6^{\text{th}}$ of its maximum output of 3.3 Volt, which equals 0.55 and 2.75 Volts, respectively. Therefore other components (e.g. a differential amplifier) will always be necessary to create a negative voltage.

External D/A Converter Instead of using the Arduino's build-in DAC, the AD669 D/A converter from Analog Devices is used because of its desired bipolar output range of -10 V to +10 V. The data is loaded into the AD669 in a parallel 16-bit format.

External A/D Converter The capacitive sensor has a bipolar output of -10 V to +10 V to describe a position between 25 and 75 μm . This analog signal is converted at a sampling rate of 10^5 samples per second to a 16 bit digital signal by the LTC1605 A/D converter of Linear Technology.

Both the A/D and D/A converter were connected to the Arduino using custom build PCB's.

Current Amplifier

The (inverting) current amplifier (see Figure H.1) is very similar to the non-inverting current amplifiers used in the 6-DoF stage. Therefore, for further reading on all the components see Chapter 6. The gain of this non-inverting amplifier is:

$$G = -\frac{R_2}{R_1 \cdot R_3} \quad (\text{H.1})$$

with $R_1 = 13 \text{ k}\Omega$, $R_2 = 1 \text{ k}\Omega$ and $R_3 = 1 \Omega$. This results in a gain of $-\frac{1}{13}$ A/V. The maximum output voltage is 10 V, so a maximum force of 1.3 N can be delivered to the stage.

A downside of this inverting amplifier is that its behaviour changes when a different ratio of R_1 and R_2 is chosen. The non-inverting amplifier of Chapter 6 does not have this problem.

Controller

The system is controlled following the rules of thumb as described by Munnig Schmidt [22]:

$$k_p = \frac{1}{3}m\omega_{BW}^2 \quad k_i = 60k_p \quad k_d = \frac{3k_p}{\omega_{BW}} \quad T_f = \frac{1}{3.3}\omega_{BW}$$

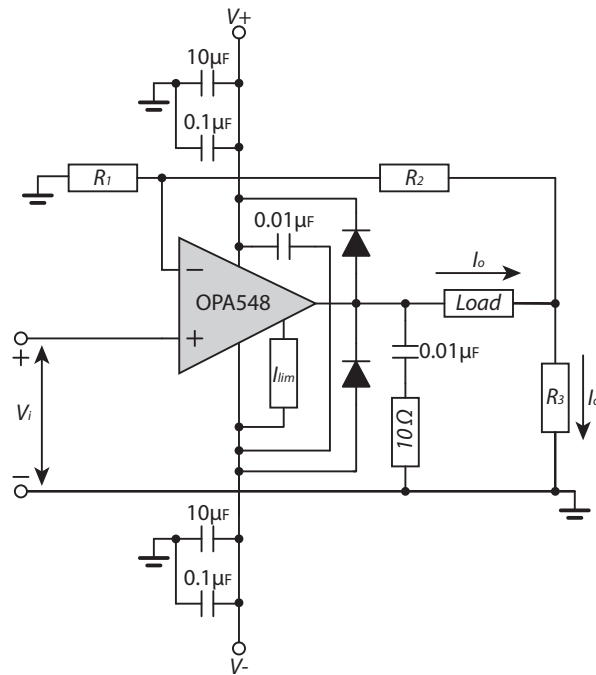
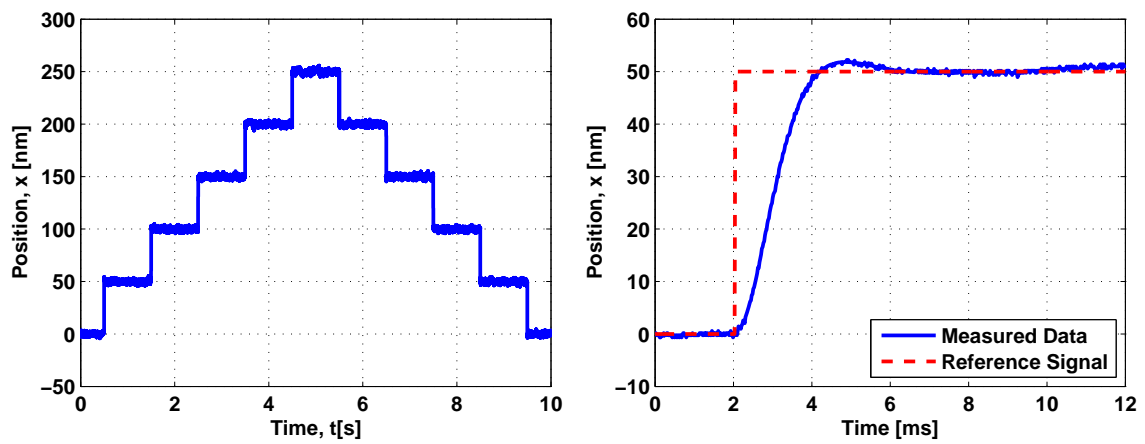


Figure H.1: Inverting Current Amplifier

The controller hardware is an Arduino Due with a clock speed of 84 MHz. The full control loop had a cycling frequency of 15 kHz. With a control bandwidth of 300 Hz a precision of 1.6 nm was achieved. The step response is shown in Figure H.2.



(a) Multiple Steps

(b) Single Step

Figure H.2: Step response of the improved 1-DoF ferrofluid stage. The risetime is 1.3 ms and the precision is 1.6 nm (σ).

Appendix I

PCB connector and pin-out

A D-sub 15 (DA-15) connector is mounted on the PCB. The other end of the cable is connected to the 6-in-1 current amplifier. Further reading on the current amplifier can be found in chapter Chapter 6. The connector pin-out is listed in table I.1, it is also listed on the top of the PCB.

Table I.1: D-sub DA-15 connector pin-out

Pin	Connection	Pin	Connection
1	In-Plane Coil 1, positive	9	Vertical Coil 1, positive
2	In-Plane Coil 1, negative	10	Vertical Coil 1, negative
3	In-Plane Coil 2, positive	11	Vertical Coil 2, positive
4	In-Plane Coil 2, negative	12	Vertical Coil 2, negative
5	In-Plane Coil 3, positive	13	Vertical Coil 3, positive
6	In-Plane Coil 3, negative	14	Vertical Coil 3, negative
7	Ground	15	Ground
8	Ground		

Bibliography

- [1] A. van Beek, *Advanced Engineering Design: Lifetime Performance and Reliability*. TU Delft, 2006.
- [2] S. Earnshaw, “On the nature of the molecular forces which regulate the constitution of the luminiferous ether,” *Trans. Camb. Phil. Soc.*, vol. 7, pp. 97–112, 1842.
- [3] R. Rosensweig, R. Kaiser, and G. Miskolczy, “Viscosity of magnetic fluid in a magnetic field,” *Journal of Colloid and Interface Science*, vol. 29, no. 4, pp. 680 – 686, 1969.
- [4] E. Mozgovoï, E. Y. Blum, and A. Tsebers, “Ferromagnetic fluid flow in magnetic fields,” *Magn. Hidrodin.*, vol. 1, no. 1, pp. 61–67, 1973.
- [5] E. Kneller, A. Seeger, and H. Kronmüller, “Ferromagnetismus,” in *Ferromagnetismus*, pp. 30–37, Springer Berlin Heidelberg, 1962.
- [6] K. Raj and R. Boulton, “Ferrofluids, properties and applications,” *Materials & Design*, vol. 8, no. 4, pp. 233–236, 1987.
- [7] S. Odenbach, “Recent progress in magnetic fluid research,” *Journal of Physics: Condensed Matter*, vol. 16, no. 32, p. R1135, 2004.
- [8] W. Ochonski and L. Kren, “The attraction of ferrofluid bearings,” *Machine design*, vol. 77, no. 21, pp. 96–99, 2005.
- [9] R. E. Rosensweig, *Ferrohydrodynamics*. Courier Dover Publications, 1998.
- [10] T. Osman, G. Nada, and Z. Safar, “Static and dynamic characteristics of magnetized journal bearings lubricated with ferrofluid,” *Tribology International*, vol. 34, no. 6, pp. 369 – 380, 2001.
- [11] M. Miwa, H. Harita, T. Nishigami, R. Kaneko, and H. Unozawa, “Frequency characteristics of stiffness and damping effect of a ferrofluid bearing,” *Tribology Letters*, vol. 15, no. 2, pp. 97–105, 2003.
- [12] K. Raj, Y. Hirota, and T. Black, “Current and emerging applications of ferrofluids,” *Magneto hydrodynamics (0024-998X)*, vol. 49, 2013.

-
- [13] G. Millet, A. Hubert, *et al.*, “Design of a 3 dof displacement stage based on ferrofluids,” in *10th International Conference on New Actuators and 4th International Exhibition on Smart Actuators and Drive Systems*, pp. 656–659, 2006.
- [14] D. Morsink, D. Liefferink, L. Lanphen, and M. Fekkes, “Ontwerp van een usb microscooptafel.” BSc. Thesis, 2011.
- [15] S. van Veen, “Planar ferrofluid bearings for precision stages,” Master’s thesis, Delft University of Technology, 2013.
- [16] M. Born and E. Wolf, *Principles of optics: electromagnetic theory of propagation, interference and diffraction of light*. CUP Archive, 1999.
- [17] E. I. Rivin, “Vibration isolation of precision equipment,” *Precision Engineering*, vol. 17, no. 1, pp. 41–56, 1995.
- [18] C. G. Gordon, “Generic criteria for vibration-sensitive equipment,” in *San Jose-DL tentative*, pp. 71–85, International Society for Optics and Photonics, 1992.
- [19] R. Li, “Optimization of thermal via design parameters based on an analytical thermal resistance model,” in *Thermal and Thermomechanical Phenomena in Electronic Systems, 1998. IThERM’98. The Sixth Intersociety Conference on*, pp. 475–480, IEEE, 1998.
- [20] EuroCircuits, “Panel guidelines,” January 2010.
- [21] A. Herczyński, “Bound charges and currents,” *American Journal of Physics*, vol. 81, no. 3, pp. 202–205, 2013.
- [22] R. Munnig Schmidt, G. Schitter, and J. van Eijk, *The Design of High Performance Mechatronics: High-tech Functionality by Multidisciplinary System Integration*. Delft University Press, 2011.
- [23] R. Murray, Z. Li, S. Sastry, and S. Sastry, *A Mathematical Introduction to Robotic Manipulation*. Taylor & Francis, 1994.
- [24] K. J. Åström and T. Hägglund, “Pid control-theory, design and tuning,” *Instrument Society of America, Research Triangle ParN, NC,*, 1995.
- [25] S. Bennett, *A history of control engineering, 1930-1955*. No. 47, IET, 1993.
- [26] V. Rankov, R. J. Locke, R. J. Edens, P. R. Barber, and B. Vojnovic, “An algorithm for image stitching and blending,” *Proc. SPIE*, vol. 5701, pp. 190–199, 2005.
- [27] A. Olszak, J. Schmit, and M. Heaton, “Interferometric approaches each have advantages,” *Laser Focus World*, vol. 37, no. 9, pp. 93–95, 2001.
- [28] P. Hariharan, *Basics of Interferometry*. Academic Press, 2010.
- [29] S. Woods, “Understanding scanning white light interferometry,” *Micromanufacturing*, vol. 2, december 2009.
- [30] J. Jackson, *Classical Electrodynamics*. Wiley, 1999.

